

Review

# Multiscale Frictional Properties of Cotton Fibers: A Review

Farzad Hosseinali \* and J. Alex Thomasson

Department of Biological and Agricultural Engineering, Texas A&M University, College Station, TX 77843, USA; thomasson@tamu.edu

\* Correspondence: fhossein@tamu.edu

Received: 3 May 2018; Accepted: 9 July 2018; Published: 13 July 2018



**Abstract:** This review discusses the important concept of cotton fiber friction at both the macro- and nanoscale. First, the technological importance of fiber friction and its role in fiber breakage during fiber processing is discussed. Next, previous studies on frictional properties of cotton fibers are reviewed and different experimental procedures to measure friction between fibers or against another surface are evaluated. Friction models developed to explain friction process during various experimental procedures are considered and their limitations are discussed. Since interpretation of friction processes at the macroscale can be challenging (mainly due to difficulties in analyzing the multiple asperities in contact), a separate section is devoted to surveying studies on the emerging field of single-asperity friction experiments with atomic force microscope (AFM). Special attention is given to studies on nanoscale frictional characteristics of rough viscoelastic surfaces (e.g., plant cuticular biopolymers and cotton fibers). Due to the close relationship between friction and adhesion hysteresis at the nanoscale, adhesion studies with AFM on viscoelastic surfaces are also reviewed. Lastly, recommendations are made for future research in the field of frictional properties of cotton fibers.

**Keywords:** cotton fiber; lint cleaner; fiber friction; nanoscale friction; adhesion

---

## Table of Contents

1. Technological Importance of Friction in Ginning Process	1
1.1. Fiber Breakage in Lint Cleaning	2
1.2. Friction as a Key Factor	4
2. Macroscale Friction Laws	5
2.1. Friction Laws for Elastic Materials	5
2.2. Friction Laws for Viscoelastic Solids	6
2.3. Friction Models for Textile Fibers	6
2.4. Howell's Friction Law Conditions	8
2.5. Studies on Cotton Fiber Friction	9
3. Nanoscale Friction and Adhesion	13
3.1. Nanoscale Friction on Viscoelastic Surfaces	13
3.2. Nanoscale Adhesion on Viscoelastic Surfaces	17
3.3. Nanomechanical Properties of Plant Tissues	20
3.4. Nanofrictional and Nanomechanical Properties of Cotton Fibers	21
4. Future Research	21
References	22

## 1. Technological Importance of Friction in Ginning Process

Processing of seed cotton into fiber and seed is generally referred to as ginning. An industrial scale ginning facility is composed of multiple unit operations such as a feed control system, dryers, cylinder cleaners, stick machines, extractor feeders, gin stands, lint cleaners, and baling press machines [1]. The importance of monitoring the fiber quality parameters throughout different stages of a ginning operation should be strongly emphasized. Different online sensors have been developed and commercialized to control main ginning operation parameters such as the real-time cotton mass flow, the quantity of impurity particles, and the level of fiber moisture content. In comparison, the number of studies concerning the development of in-situ fiber physical properties measurements with potential application in ginning processes is limited. Some of these studies are as follows. Thomasson et al. measured the reflectance of different cotton samples at near infrared (NIR) wavelengths. They showed that ratios of NIR bands are strong predictors of micronaire and length [2]. By applying similar methodology, Sui et al. developed an image-based optical sensor to estimate the cotton micronaire value [3]. Shahriar et al. developed an imaging system, based on the transfer learning approach, with the capability to measure both length and average maturity of individual fibers from their longitudinal images [4]. It was found that sensors can be developed based on image processing algorithms to more precisely monitor fiber quality parameters throughout different stages of fiber processing.

The two main purposes of the overall ginning process are to separate fibers from their seeds, and to improve the composite grade of cotton by removing impurity particles entrapped within masses of fibers. While performing these tasks, special care is taken by cotton ginners to avoid fiber damage and to preserve fiber length characteristics. Nevertheless, it is well-documented that the ginning operation breaks some fibers and degrades the mean fiber length [5–11]. Hosseinali showed that within a sample of processed cotton fiber, shorter fibers have lower tensile strength on average [11]. This indicates that throughout a harsh ginning processing, longer fibers with low tensile strength break into shorter fibers, leading to an increase in percentage of short fibers with low tensile strength. Research has shown that fiber damage is strongly dependent on the sequence of cleaning and ginning machines, settings of the machines, moisture content of fibers during processing, the type of impurities, heating conditions, and inherent physical properties of fibers—which depend on the cotton variety and environmental factors during the growing season. For this reason, ginning machines, which can potentially degrade fiber quality, need to be studied and analyzed in more detail with respect to their effects on fiber quality.

### 1.1. Fiber Breakage in Lint Cleaning

One of the main unit operations in cotton ginning is lint cleaning, which is commonly done with a controlled batt-saw-type lint cleaner (SLC) [12]. Lint cleaning is defined as any dry process related to the release of large foreign matter and fine dust particles from the cotton fiber mass with mechanical and/or pneumatic actions. SLC machines are installed immediately after the gin stand or another lint cleaning machine (either SLC or flow-through lint cleaner). An SLC consists of a fiber condenser drum, a controlled-batt feed mechanism, a saw-wire-wrapped cylinder, a set of grid bars around the saw cylinder, and an air suction doffing system (Figure 1). The performance of an SLC machine is often evaluated by variables such as cleaning efficiency, lint wastage, lint turnout, and reductions in fiber quality (known as fiber damage). Cleaning efficiency is determined by measuring the foreign matter content of a fiber sample before and after the lint cleaning process. Lint wastage is a measure of the fibrous portion of waste material removed by an SLC machine. Changes in fiber quality are calculated by measuring certain fiber quality parameters of the fiber sample before and after the lint cleaning process. A desirable lint cleaning process is considered to be the one that removes a maximum of impurity particles (high efficiency) while preserving the fiber length characteristics (low lint damage and wastage). As reported by Sui et al. and Hughs et al., although harsh lint cleaning operations

increase lint cleaning efficiency, they negatively impact fiber quality parameters by degrading the average fiber length [11], and increasing both the short fiber content (SFC) and the nep content [13,14].

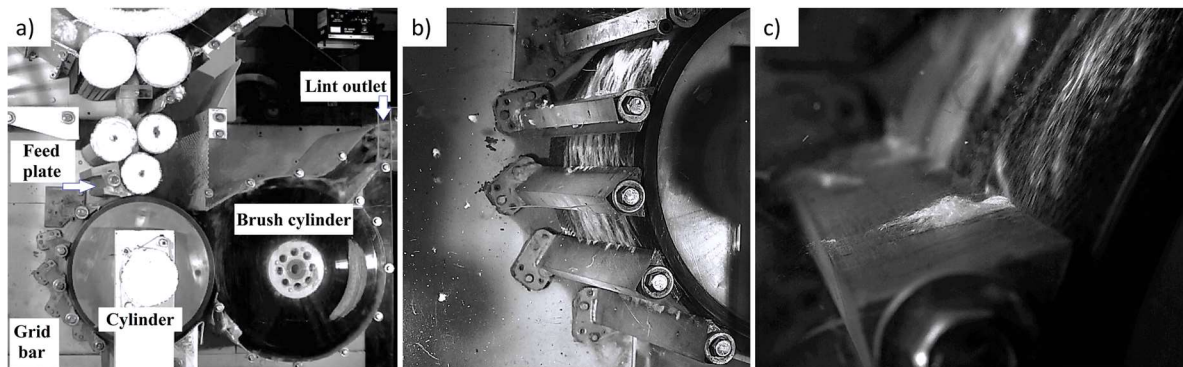


**Figure 1.** (a) Different components of lint cleaner machine; (b) set of grid bars inside lint cleaner; (c) interactions between fiber and grid bar.

Two major forces are applied to fibers in lint cleaning which may cause fiber breakage [15,16]: (i) tensile forces along the fiber axis as they are seized by a saw tooth and (ii) frictional force on fiber surfaces as they rapidly travel around the edge of a feed plate. Therefore, the manner in which fibers are delivered to the cylinder is a critical mechanical procedure that determines largely both the cleaning efficiency and the fiber damage. As the cylinder tooth and the fibers attached to it continue to rotate with the approximate linear velocity of 20 m/s, the fiber tuft will be dragged and scrubbed against eight sharp-edge grid bars. Two primary purposes of grid bars are to separate impurity particles from fibers and to deflect fibers to remain on the saw cylinder. The fiber-grid bar interaction can be divided into four continuous steps. In step one, before fibers approach the grid bar, centrifugal forces with respect to the axis of rotation cause slight elevation of the fibers from the cylinder surface (Figure 2a). Impurity particles with more mass have more centrifugal force acting upon them. As a result, large impurity particles and some poorly attached fibers are separated by centrifugal force. In step two, the middle section of the fiber tuft impacts against the edge of the grid bar (Figure 2b). In step three, the tuft rapidly slides over the grid bar under normal pressure due to the centrifugal forces (Figure 2c). Shear stresses applied to the tuft in this step have a tendency to restrain the movement of the tuft. Once a foreign particle encounters the grid bar edge, it functions as a surface impurity or a bump compared to the flat surface of the fibrous assembly. Therefore, since there is more contact area and interaction between the particles and the stiff grid bar, frictional forces acting on them are higher. In the case where the sum of these resistance forces is high compared to the forces holding the particle inside the assembly, the particle will be detached from the tuft to dissipate the frictional energy. As a result, the particle rebounds from the grid bar and is separated from the tuft. The same thing can be said for individual fibers within fiber tufts; that is, if a significant amount of frictional force is applied to fibers by grid bars, they are either separated from the tuft or break into smaller segments. In step four, fibers travel past the grid bar (Figure 2d). At the end of the lint cleaning process, straightened fibers are collected from the saw cylinder by the collector brush. After that, fibers are transported to the next stage of the ginning operation via air current. Throughout a lint cleaning process, pneumatic, tensile, centrifugal, and frictional forces are applied to fibers. Among these, tensile and high-speed frictional forces cause fiber breakage and damage. Nevertheless, to the best knowledge of the author of this article, no research paper has been published on surface roughness of fiber assemblies and its impact on frictional forces between fibers and the SLC grid bars.

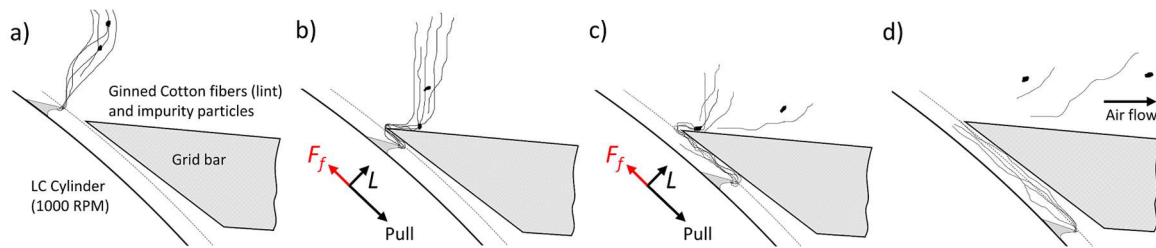


**Figure 2.** Mechanism of the fiber–grid bar interaction: (a) fiber tuft is elevated from the cylinder surface due to centrifugal forces; (b) the middle section of the fiber tuft impacts against the edge of the grid bar; (c) the tuft rapidly slides over the grid bar; (d) the fiber tuft travels past the grid bar while impurity particles rebound from it.

### 1.2. Friction as a Key Factor

SLC design and developments have been more based on trial and error methods than science. Researchers have been trying to optimize the effect of the SLC design factors in order to achieve maximum cleaning efficiency and retain fiber qualities. Modification and optimization of design factors alter the magnitude of forces and interactions between fibers and machine parts. Some of the published studies on this subject are summarized here. Baker et al. reported that changes in the batt weight, the combing ratio, and the saw speed did not have any major impact on fiber quality measurements [17,18]. However, they significantly influenced both lint wastage and cleaning efficiency. Baker et al. later studied the effect of the combing ratio on fiber quality measurements and open-end spun yarn properties [19]. Their results showed that increasing the combing ratio from 25 to 50 significantly reduced the 2.5% span length and the upper quartile length; nevertheless, the yarn properties were not affected in a major way. Leonard et al. compared the performance of notched-edge grid bars against regular plain-edged ones [20]. Any modification in grid bars design alters the scrubbing forces applied to fiber tufts. However, they reported that the indentation of the grid bars edge did not affect the level of fiber damage significantly. Columbus studied influences of four saw cylinder speeds and the saw tooth density on fiber quality parameters and the SLC cleaning efficiency [21]. His results showed that, at a constant combing ratio, an increase in the saw cylinder speed did not affect the upper-half mean length. However, increasing the saw tooth density significantly reduced the upper-half mean length. Baker et al. studied effects of the spacing between grid bars, the curvature radius of grid bars front edge, and the clearance distance between grid bars and the saw teeth on cleaning performance and fiber quality measurements [22]. Their results indicated the studied variables had no significant effect on high volume instrument (HVI<sup>TM</sup>) parameters. The sharp edge grid bars, however, produced better fiber length distributions as measured by the array method. Mangialardi modified an SLC machine by reversing its feed plate and mounting a round lint-saver bar and a carding brush ahead of the first grid bar [23]. By reversing the feed plate, less frictional shear stresses are placed on fibers since they do not have to travel around the edge of the feed plate once a saw tooth seizes them. His study showed that, although reversing the feed plate improved the fiber quality preservation, it reduced the cleaning performance of the machine. The effects of the round lint-saver bar and the carding brush on fiber quality were not significant. He concluded that the action of fiber and grid bar have a greater impact on the impurity particle removal process than the action of fiber and feed plate. Le studied the effects of saw speed, feed rate, combing ratio, and moisture content on the fiber damage [24]. He concluded that fibers with lower moisture content experienced significantly more breakage throughout the lint cleaning processing. According to his study, the changes in machine settings caused no significant effect on the typical level of fiber damage imparted by the SLC. Gordon et al. used a laboratory scale SLC and investigated the effects of various lint cleaning elements on fiber quality by eliminating them from the machine [25]. They concluded that the majorly of fiber damage in a SLC takes place when fibers are being delivered from the feed plate onto the saw cylinder. This literature review indirectly shows that the modification of fiber and

machine parts interactions—mostly in the form of alteration in frictional forces between fibers and the grid bars or fibers and the feed plate—impacts the magnitude of fiber breakage and damage during the lint cleaning operation.

In addition to machine settings, inherent physical properties of fibers also affect the performance of fibers during a lint cleaning operation. Dever et al. studied the effects of fiber properties on the extent of fiber breakage during ginning operations [26]. They reported that the fiber breakage in the saw ginning and the lint cleaning processes was better correlated with fibers strength and fineness, respectively. Their results showed that, throughout the ginning operation, the finer and stronger fibers from the *Gossypium barbadense* cultivar incurred less damage compared to the coarser and weaker ones from the *Gossypium hirsutum* type. Their study on relationships between fiber properties and nep formation showed that the final nep count after ginning was significantly correlated with fiber maturity. However, the tendency of fibers to entangle into neps during the ginning operation was reported to be more correlated with the flexural rigidity of fibers—as determined by their length and fineness—and the amount of foreign matter content. Mangialardi et al. reported that both variety and the degree of mechanical lint cleaning significantly impacted the final nep count [27]. Their results showed that the varieties with lower nep counts were also associated with higher micronaire values. Hughs et al. conducted a similar type of experiment on seven varieties and four level of lint cleaning [28]. Their results showed that the nepping potential of cotton fibers varies significantly across different varieties and the lint cleaning treatment. These studies signify the influence of the inherent fiber quality parameters on the level of fiber damage during the lint cleaning process. Since significant frictional forces are applied to fibers during lint cleaning, the surface roughness of individual fibers and fiber assemblies are certainly among those inherent fiber quality parameters that directly influence fiber damage in this unit operation.

## 2. Macroscale Friction Laws

Materials friction affects many industrial waste issues such as large-scale energy dissipation and material losses taking place at contacting interfaces. Friction is defined as the force resisting the relative motion of solid surfaces sliding against each other [29,30]. In the simplest scenario, when two relatively smooth surfaces slide past each other, molecules at the surface of materials collide with one another (interfacial friction) and, as a result, kinetic energy will be transferred between them. This energy will be distributed among their internal molecules as random motion or heat. In real life examples, the fraction of the energy transferred between sliding surfaces is influenced by the extent of intermolecular attractive forces (adhesion force) and existence of a lubricant film layer between the surfaces (boundary or thin film lubrication).

### 2.1. Friction Laws for Elastic Materials

Frictional force between dry metallic solids obeys the Amontons' law. That is, the friction force  $F_f$  between two macroscopic bodies is linearly proportional to the applied load  $L$ :

$$F_f = \bar{\mu}L \quad (1)$$

Here,  $\bar{\mu}$  is the macroscopic coefficient of friction which can be defined both from Equation (1), as  $\bar{\mu} = F_f/L$ , or as a slope in the  $F_f$  vs.  $L$  plot such that  $\bar{\mu} = dF/dL$ . The coefficient of friction can be measured in either static or dynamic states. The static friction coefficient  $\mu_s$  determines the lateral force needed to initiate relative motion and is typically larger than the coefficient of kinetic friction  $\mu_k$  that corresponds to the force needed to continue the motion. Amontons' law is still widely applied to nonadhering and unlubricated contact systems. However, this geometrical interpretation of friction breaks down when surfaces are in adhesive contact or when a liquid film separates them. In order to

consider the effect of adhesive bonds on the friction force of smooth surfaces, it has been suggested to modify Amontons' equation to the following form [31]:

$$F_f = \bar{\tau}A_{real} + \bar{\mu}L \quad (2)$$

Here,  $\bar{\tau}$  is the effective shear strength of contacting bodies at the real contact area  $A_{real}$ . The first component of Equation (2) accounts for the adhesion-controlled impact (friction force at zero load) and is related to the intermolecular forces between surfaces. The second component accounts for the load-controlled impact and is related to the structure and topography of surfaces. A macroscopic contact, with the apparent contact area of  $A_{apparent}$ , is rough and consists of  $n$  number of smaller contacts. If we denote the contact area of the asperity  $i$  by  $A_i$ , so that  $A_{real} = \sum_{i=1}^n A_i$ , then Equation (2) can be rewritten as:

$$F_f = \bar{\tau} \sum_{i=1}^n A_i + \bar{\mu}L, \quad (3)$$

At low loads, the friction force is mostly adhesion-controlled. At high loads, irrespective of the relationship between load and real contact area, the friction force is dominated by the load-controlled impact.

## 2.2. Friction Laws for Viscoelastic Solids

Friction, adhesion, and wear of polymer materials have long been studied [32–34]. Specifically, the tribological properties of conventional bulk plastics [35–38], rubber-like materials [39], fiber-reinforced composites [40], polymer nanocomposites [41–43], cross-linked hydrogels [44], end-grafted polymers (a.k.a. polymer brushes) [45], mammalian articular joints [46], gecko-inspired surfaces [47], and mussel-inspired coatings [48] have been investigated. For viscoelastic solids, such as polymers, it has been shown that friction is velocity-dependent and Equation (1) cannot be valid over a wide range of sliding velocities. In fact, the plot of  $F_f$  vs.  $L$  is often used for various viscoelastic materials to analyze their energy dissipating mechanisms underlying the friction process. Therefore, for polymers, the coefficient of friction is material-dependent and influenced by both the sliding velocity and the real contact area (especially, at low normal loads).

The polymer sliding friction mechanism may consist of two components: the deformation component,  $F_d$ , and the adhesion component,  $F_a$  [29,32]. The relative contributions of these components are influenced by surface roughness, polymer viscoelasticity, the sliding velocity, temperature, moisture content, and lubricity of contacting materials. The deformation component arises due to the plowing of asperities of a harder solid through a softer one. Once two rough surfaces slide against each other, if the contact pressure exceeds the yield stress of the junctions, the softer material will deform and will pile up ahead of asperities of the rigid material. This phenomenon is mainly governed by the viscoelastic energy dissipation characteristics of the bulk polymers near deforming asperities. The deformation component is therefore proportional to the energy of plowing and affected by the normal load according to the following equation:

$$F_d = c(L)^n \tan \delta \quad (4)$$

where  $c$  and  $n$  are constant and  $\tan \delta$  is the tangent loss, a variable accounting for the internal friction between polymer chains. Equation (4) indicates that the deformation component is affected by the internal friction within a bulk of polymer [39]. The adhesion component, however, is affected by the surface energetics parameters of the polymer and is proportional to the shear strength and the real contact area of the contacting asperities:

$$F_a = \bar{\tau}A_{real} \quad (5)$$

### 2.3. Friction Models for Textile Fibers

Several friction models have been proposed to describe the relationships between the friction force, the contact area, and the normal load when fibrous materials slide past each other or another surface (Figure 3) [49–53]. Often these models have been used by researchers to explain their contact system of interest without proper knowledge of the origin of these models and the particular assumptions that have to be made. The purpose of this section is to briefly review these models and highlight related assumptions.

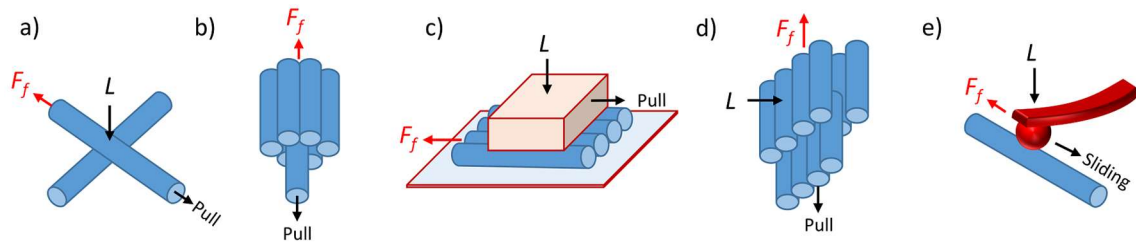


**Figure 3.** Different experimental procedure used for measuring fiber friction: (a) two crossed fibers; (b) single fiber withdrawing; (c) Sliding friction; (d) fiber fringe (combed nearly parallel fibers); (e) colloidal force microcopy.

Manmade textile fibers are produced from synthetic polymers with well-defined fiber cross-section shape and dimensions. Frictional forces opposing the relative motion of a fiber with respect to its adjacent fibers or another surface can be explained by two mechanisms: adhesion (over the contact area) and viscoelastic surface deformation (or plowing). The friction laws of polymeric surfaces were first applied to the study of friction between textile fibers by Howell [49–51]. Under the assumptions of insignificant surface roughness and zero plowing, he proposed the following equation for friction between two crossed fibers (Figure 3a):

$$F_f = aL^n \tag{6}$$

where  $a$  and  $n$  are constants depending on the fiber type. In the case of contact between two smooth cylindrical surfaces, the theoretical values of the parameters  $a$  and  $n$  depend on the shear breaking strength, mechanical properties, and dimensions of the cylinders. Equation (6) can be derived from the famous Hertz contact theory in the contact region between the two elastic solid spheres. Under Howell’s assumptions, friction is only proportional to the shear strength of the junctions and the real area of contact such that:

$$F_f = \bar{\tau}A_{real} \tag{7}$$

The real contact area for two crossed cylinders is in the shape of a circle with radius  $a$ . If we assume that the fibers deform in Hertzian regime, the real contact area can be measured as a function of normal force by:

$$a = \sqrt[3]{\frac{RL}{E_{tot}}} \tag{8}$$

Therefore, Equation (3) takes the following form:

$$F_f = \bar{\tau}\pi\left(\frac{RL}{E_{tot}}\right)^{\frac{2}{3}} \tag{9}$$

Here,  $R$  is the effective radius, defined as  $\frac{1}{R} = \frac{1}{R_1} + \frac{1}{R_2}$ , where  $R_1$  and  $R_2$  are the radii of circular cross-sections of the fibers. Equation (9) can take the following general form:

$$F_f = \bar{\tau}KL^{\frac{2}{3}} \tag{10}$$

Here,  $K$  is a constant repressing the stiffness and the size of fibers. By comparing Equations (6) and (10) the theoretical values for  $a$  and  $n$  are  $a = \bar{\tau}K$  and  $n = 2/3$ . As can be seen, the parameter  $a$  is a general term, with the dimension of  $[force]^{1-n}$ , which is different from the dimensionless friction coefficient  $\mu$  in Equation (1). The value of  $n = 0.67$  is obtained for fully elastic deformation. Howell noted that for pure plastic deformation,  $n$  reaches unity and Equation (6) becomes identical with the Amontons' law of friction  $F_f = \bar{\mu}L$ . For viscoelastic materials such as textile fibers, the index  $n$  is intermediate between 0.67 and 1.0. Equation (6) has been employed experimentally on various fibers. For drawn nylon and cellulose acetate fibers,  $n$  was measured to be 0.80 and 0.96 respectively [49,50]. Lincoln, however, reported the value of  $n = 0.67$  for nylon fibers [54].

Gupta and El-Mogahzy published a friction model based on Archard's multiple asperities contact approach [52,53]. In Archard's model, spherical asperities with similar radius of curvature are evenly distributed over the surface of a larger elastic sphere. It was shown by Archard that with an increasing number of asperities  $m$  per unit area,  $A_{real}$  becomes linearly proportional with  $L$ , and frictional forces obey Amontons' law [55]. According to Gupta et al., the total area of real contact in the case of uniform stress distribution can be obtained as:

$$A_{real} = K^{-\beta} m^{1-\beta} L^{\beta} \quad (11)$$

where  $K$  represents the stiffness or the hardness factor and  $\beta = 1/(\alpha + 1)$ . The constant  $\alpha$  is a shape factor in the pressure-area relationship as denoted by  $P = KA^{\alpha}$ . Here,  $P$  is the pressure. In the case of spherical stress distribution, the total area of real contact is expressed as:

$$A_{real} = \left[ \frac{3^{\beta} 2^{1-\beta}}{\beta + 2} \right] K^{-\beta} m^{1-\beta} L^{\beta} \quad (12)$$

They further generalized their model to the following form:

$$A_{real} = C_M K^{-\beta} m^{1-\beta} L^{\beta} \quad (13)$$

Here,  $C_M$  is a constant related to the nature of the stress distribution. Using this model, they were able to describe the  $a$  and  $n$  indices in Equation (6) in terms of the mechanical properties of asperities and the number of asperities in contact.

In addition to the aforementioned models, several other studies have been conducted to study the frictional properties of textile yarns using the Capstan equation, in which the yarns are modeled as traveling around a pin or a cylinder; these yarn models are outside the scope of this review.

#### 2.4. Howell's Friction Law Conditions

Equation (6) was developed in the 1950s by Howell and gained popularity for the study of fiber friction [32]. Since then, it has been the basis of modern nonlinear friction theories between non-adhesive surfaces at the micro and nanoscale [56]. With developments in Surface Force Apparatuses (SFAs), it is possible to collect both single asperity friction and contact area empirical data between two crossed cylinders coated with materials of interest [57]. With SFAs, data on friction and contact area as a function of applied load can be fit to Equation (10) by adjusting the  $a$  and  $n$  indices or by inserting some known values for both  $n$  and  $K$  and solving for  $\bar{\tau}$ . While Equation (10) is easy to execute and interpret, care must be taken in fitting this equation for study of various contact problems. The key conditions that have to be met are as follows:

(i) The sublinear relationship between  $F_f$  and  $L$  holds only in the case of microscale point contacts between smooth fibers under very light normal pressures. Upon the occurrence of surface damage and the formation of wear debris between the surfaces, friction will be dominated by  $F_f = \bar{\mu}L$ . In the study of macroscale friction under relatively high normal force, surface damages and plastic deformation

are unavoidable; therefore Amontons' law of friction is found to be a more accurate fit for macroscale friction experiments of bulk materials [31].

(ii) Howell's assumptions of nominally flat surfaces and fibers circular cross-section can be easily violated. For instance, natural fibers, such as desiccated cotton fibers, have nanoscale surface roughness and irregular cross-section shape that can alter the stress distribution inside the contact region and affect the real contact area between the contacting surfaces. According to Archard, and later Greenwood, the validity of Amontons's friction law for a given surface also depends on its surface roughness [55,58]. Although  $F_f \propto L^{2/3}$  for an elastic single-asperity contact, it has been shown that the value of index  $n$  tends to reach unity for a rough multiasperity contact.

(iii) One should also consider the effect of environmental conditions on experimental results. Specifically, in the study of biological materials, the outermost layer of the plant cell wall often consists of various amounts of polysaccharides and fatty acids. The polysaccharide constituent of the primary cell wall is a hydrophilic structure, meaning that if contact experiments are not conducted under low humidity, a water meniscus can be formed between the crossed fibers. This water meniscus will affect the overall interfiber friction forces.

(iv) In the case of two parallel fibers in contact or a fiber in contact with a flat surface, the contact area is no longer circular. In these cases, the contact area is a rectangle with length  $l$  and width  $2b$ . With Hertz theory, the half-width  $b$  and the corresponding friction force in the direction of fiber axis are defined as follows:

$$b = \sqrt{\frac{4RL_l}{\pi E_{tot}}} \quad (14)$$

$$F_f = 4\bar{\tau}l \sqrt{\frac{RL_l}{\pi E_{tot}}} \quad (15)$$

Here,  $L_l$  is the normal force per unit length of  $l$  and  $F_f \propto L_l^{1/2}$ . More recently, Cornelissen et al. have employed the Hertz theory, Equations (8) and (14), to quantify the real contact area between two contacting carbon fibers with different crossing angles [59,60]. In the case where the fibers are not oriented perpendicular or parallel to each other, the contact area is an ellipse with semi-minor and semi-major axes. The area of an elliptical contact geometry can be also predicted by employing the Hertz contact model.

(v) Equation (10) assumes Hertzian deformation at the point of contact between two crossed cylinders. In the Hertzian theory, as previously mentioned, the intermolecular attractive forces between the two surfaces are neglected. The Jonson–Kendall–Roberts (JKR) model corrected the Hertz approach by considering attractive forces between surfaces in the form of work-of-adhesion  $W$  [61]. By replacing the contact area component in Equation (7) with the corresponding JKR component, the friction force at the point of contact between two crossed cylinders (fibers) with adhesion can be measured as:

$$F_f = \bar{\tau}\pi \left( \frac{R}{E_{tot}} \left( \sqrt{\frac{3}{2}\pi RW} + \sqrt{L + \frac{3}{2}\pi RW} \right)^2 \right)^{\frac{2}{3}} \quad (16)$$

Although the JKR model is well-developed for spherical contact geometries, limited work has been conducted on the study of JKR-type contact deformation between parallel cylindrical surfaces or a smooth cylinder in contact with a flat surface.

## 2.5. Studies on Cotton Fiber Friction

Frictional properties of cotton fibers have been reviewed extensively [62]. Figure 4 shows images of unprocessed cotton fibers at different length scales. Various books and book chapters are available on this topic. However, ambiguity still exists in fiber friction experimental techniques and interpretation of fiber friction results. On the study of cotton fiber friction, most experiments have been performed

on frictional forces between groups of fibers rather than individual fibers. This is partially due to the difficulties associated with measuring nanoscale frictional force between individual cotton fibers. However, it may also be due to the fact that the fiber bundle friction experiment provides an effective average friction measurement of a sample which reduces the error caused by variation between individual fibers. Also, fiber bundle friction results correlate better with common fiber and yarn physical properties. Following is a brief review of published studies on the subject of frictional properties of cotton fibers. These studies are also listed in Table 1.

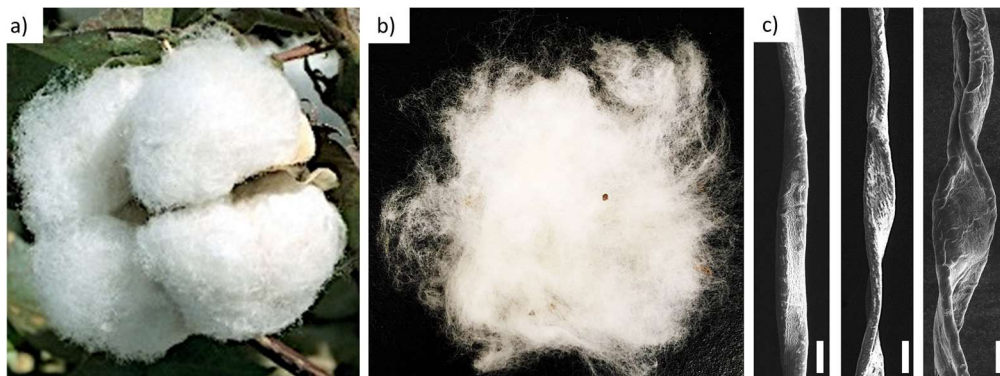


**Figure 4.** (a) Open cotton boll; (b) tuft of ginned fiber; (c) scanning electron microscopy images of individual cotton fibers.

**Table 1.** Previous studies on frictional properties of cotton fibers ordered by publication date.

First author	Experiment Type	No. of Samples	Relationship with Normal Load
K. Sen [63]	Single fiber withdrawing	17	-
E. Lord [64]	Fiber fringe (combed nearly parallel fibers)	29	$F_f = \bar{\mu}L$
W. Du Bois [65]	Fiber fringe (combed nearly parallel fibers)	12	$F_f = aL^n$
R. Belser [66]	Crossed fibers	-	$F_f = aL^n$
K. Hertel [67]	Web of fibers (large scale cardi webs)	28	$S = \frac{L K (A_0 - A_n)^2 T}{n^2 (A_0 + A_n)}$
A. Viswanathan [68]	Fiber fringe (combed nearly parallel fibers)	10	$F_f = aL^n$ and $F_f = \bar{\mu}L$
V. Subramaniam [69,70]	Fiber fringe (combed nearly parallel fibers)	17	$F_f = aL^n$
Y. El Mogahzy [52,71]	Fiber fringe (combed nearly parallel fibers)	2	$F_f = aL^n$
T. Pesacreta [72]	Morphology with AFM	1	-
Y. El Mogahzy [73]	Rotor ring	-	-
G. Gamble [74]	Rotor ring	2	-
S. Nowrouzieh [75]	Sliver cohesion	2	$F_f = aL^n$
Z. Zhang [76]	Nanofriction with AFM	1	$F_f = \bar{\mu}L$
Y. Zhang [77]	Rotating cylinder	1	$F_f = \bar{\mu}L$
F. Hosseinali [78]	Sliding friction test	48	$F_f = \bar{\mu}L$
F. Hosseinali [79]	Nanofriction with AFM	2	$F_f = aL^n$

Sen and Ahmad performed a comprehensive investigation on the effects of various fiber quality parameters and experimental conditions on what is called the clinging power of individual cotton fibers [63]. The clinging power is defined as the force necessary to withdraw a fiber along the fiber axis from between two assemblies of parallel fibers in an effort to assess the coefficient of friction of the fiber against its adjacent fibers (Figure 3b). Their results on the clinging power of seventeen different cotton varieties showed that samples with larger fiber cell diameter are characterized with higher interfiber friction. This is probably because of the larger contact area associated with these fibers. In the study of the effect of fiber convolutions on fiber friction, they reported a weak correlation between the average number of convolutions per unit length and fiber friction. They noted that the effect of convolutions on fiber friction can be masked by other significant factors such as the fiber diameter and the degree of secondary cell wall (SCW) thickness. Also, according to their results, removing the waxy layer from the fiber surface significantly increased the interfiber friction. By removing the cotton wax, the overall friction between the fibers increases because of the rougher surface of the layer underneath.

Lord compared the coefficient of friction ( $\mu = F_f/L$ ) of 29 varieties of cottons as measured by withdrawing a fringe of parallel fibers from between two other fringes (Figure 3d) [64]. He reported correlation coefficients of  $-0.806$  and  $0.609$  between  $\bar{\mu}$  and maturity and  $\bar{\mu}$  and convolutions per unit length, respectively. He explained that since mature fibers (higher degree of SCW thickness) have a rounder cross-section, it should be easier for them to slide over one another. Du Bois repeated Lord's work on 12 varieties and concluded that fibers from *Gossypium barbadense* species are associated with lower friction coefficient compared to those of from *Gossypium hirsutum* [65]. Viswanathan noted that the frictional force between fringes of fibers under low normal force is proportional to  $l/\sqrt{MH}$ , where  $l$  is the mean fiber length,  $M$  is the fiber maturity, and  $H$  is the fiber fineness [80]. For 30 different cotton varieties, he reported the correlation coefficient of  $-0.634$  between  $F_f$  and  $l/\sqrt{MH}$ . In another study on frictional properties of 10 different varieties of cotton fibers, Viswanathan found a negative correlation between yarn strength and frictional forces between fringes of fibers, again under low normal force [68]. This finding confirms that the lower fiber friction at the preparatory stages of yarn manufacturing (opening, carding, drawing, and roving) eases fiber drafting and increases the degree of cohesion in the yarn structure. However, higher fiber friction is more desirable at the final stages of yarn manufacturing (fiber spinning and twisting), where higher friction leads to better cohesion of fibers in the yarn structure. El Mogahzy et al., measured the frictional properties of HVI<sup>TM</sup> fiber beards as the fiber bundle slips between two parallel metallic plates under controlled normal pressure [71]. They compared frictional properties of Pima and Deltapine cottons and stated that both fiber/metal and fiber/fiber frictional forces are higher for the latter. Roedel et al. studied the frictional properties of cotton/polyester needle-punched nonwoven webs [81]. They explained that looping and interlocking of fibers due to the needling process caused the formation of surface protrusions. These surface irregularities on the web surface enhanced static friction and led to a pronounced stick-slip behavior.

Subramaniam et al. studied the relationships between fiber friction measured with the fiber fringe method and fiber quality parameters among seventeen different cotton samples [70]. They found significant correlation coefficients of  $-0.73$ ,  $+0.73$ , and  $-0.69$  between fiber friction and length, micronaire, and bundle strength, respectively. Based on the strong positive correlation between micronaire and fiber friction, it was concluded that interfiber friction forces are higher for coarser cottons. Subramaniam et al. also investigated the effect of fiber friction on the performance of carding and drawing unit operations [69]. For this purpose, they modified surface characteristics of fibers of a given sample by applying chemical surface treatments, such as surfactants and colloidal silica, to either reduce or enhance fiber friction to a desired amount. Their results indicated that treatment of bulk samples with surfactant decreased both card wastes and nep numbers per unit area of the card web. Treatment with colloidal silica to enhance interfiber friction, had the opposite effect. They explained that low static interfiber friction facilitates the smooth and orderly movement of fiber mass throughout different steps of fiber processing. High static interfiber friction increases the energy required for separating and disentangling fiber lumps; therefore, the probability that fibers remain in cluster form during the process will be sufficiently enhanced. In practice, in order to achieve a higher degree of lint cleaning, more energy is often consumed to open and separate such clusters, which causes an increase in both the percentages of waste products and broken fibers.

Belser et al. conducted an exclusive study on frictional properties of individual cotton fibers using the crossed fiber technique [66]. By sliding a cotton fiber over an ideal cylindrical fiber of approximately the same size, they plotted frictional forces between the two fibers as a function of the traveling distance of the moving fiber. Their results showed that the stick-slip behavior is more pronounced for cotton fibers compared to other textile fibers with circular cross-sections. They noted that the greater stick-slip peaks in the friction profile of cotton fibers are mainly due to the natural twists of the ribbon-like structure of a cotton fiber, such as convolutions and reversals. While these natural twists cause relatively high-energy static friction between fibers, once the slip occurs they reduce the mean dynamic friction by decreasing the real contact area between the fibers. Their results

showed that the large static interfiber friction of cotton fibers can be the principal driving energy for fiber travel during cotton processing under low normal forces.

Hertel developed an apparatus to measure the dissipated energy in a large assembly of cotton fibers. In this method, the fiber mass is subjected to alternating shearing forces [82]. The total energy loss during the shearing action is expressed as shear-friction. The magnitude of shear friction for a sample of cotton fibers depends upon various factors such as number of fibers in the assembly, fiber convolutions, fiber orientation, degree of entanglement, fiber crimp, length, fineness, diameter, and interfiber friction. Hertel investigated the relationship between shear-friction and other fiber physical properties of 28 different cotton bales [67]. He found a high negative correlation between mean shear-friction and both fiber upper-half mean length and mean bundle strength. He concluded that assemblies consisting of longer fiber not only tend to be stronger but also have lower shear-friction.

Fiber cohesion is defined as the resistance to separation of fibers in contact with one another. Similar to the shear-friction, this property of bulk fibrous assemblies depends on the combined effects of various fiber physical properties, including interfiber friction. The fiber cohesive force in cotton slivers can be quantified experimentally. With this technique, a known mass of cotton sliver is pulled in an axial direction, and the resisting forces are recorded with a tensile tester machine [75]. Another technique to measure the fiber cohesion is to use a RotorRing instrument [73,83–85]. The RotorRing device was originally designed to simulate different operation processes in a rotor-spinning machine. Its working principle is as follows. First, a known mass of a fiber sliver is fed to the device. Then an opening roller, which can rotate up to 3000 RPM, separates fibers from the sliver and drags them against the interior surface of a metallic casing that covers the entire opening mechanism. The energy consumed by the opening roller to separate the fibers from their bundle is called the opening energy. In a RotorRing instrument, the opening energy is measured with a torque system that is attached to the main axis of the opening roller. It is reported that, at low RPMs, the dissipated energy is mainly due to the magnitude of forces required to overcome fiber-to-fiber friction during opening action. At higher RPMs, there are more interactions between fibers and the metallic casing because of larger centrifugal forces; therefore, the dissipated energy is mainly due to the fiber-metal friction. In the next step, the individualized fibers are transported from the opening roller to the inside of a rotor with an air suction system. The rotor rotates at ~10,000 rpm. Due to the great centrifugal forces in this stage, fibers are condensed into a narrow assembly of parallel fibers (known as the fiber ring) inside the rotor wall. The thickness of the produced fiber ring is an indicator of the degree of fiber cohesion and the opening propensity of the sample fibers. Ghosh et al. used a RotorRing to study the relationship between fiber cohesion and crimp for synthetic fibers [84]. Their results showed that the higher the crimp measurement, the lower the fiber ring thickness. That is, fibers with higher crimp per unit length were more cohesive and had lower opening propensity. Their results on the opening energy of the fiber samples showed that more energy was required to open samples with higher crimp measurements; In general, fibers with higher crimp were characterized with larger fiber-to-fiber and fiber-to-metal friction. El Mogahzy et al. investigated the relationship between the opening propensity and the NIR wax content of cotton fibers using a modified RotorRing instrument [73]. They found an inverse correlation of  $-0.74$  between these two variables, meaning that cottons with higher wax content required less energy for opening. Gamble examined the effect of surface electrolyte treatment of cotton fibers on fiber-to-fiber friction [85]. He reported that any surface electrolyte treatment increased both fiber-metal and fiber-to-fiber friction.

In a recent study, Hosseinali et al. studied the frictional properties of fiber assemblies from different cotton varieties using a sliding friction tester (Figure 3c) [78]. Their Results indicated that fiber friction varies significantly across different varieties of cotton. The simple linear regression analysis showed a negative correlation between friction coefficient ( $\mu$ ) and fiber yellowness and a strong positive correlation between  $\mu$  and short-fiber content. They conducted a multilinear regression analysis to identify fiber features that significantly affect fiber friction. Their analysis revealed that fiber friction is a complex surface phenomenon that depends on fiber dimensional, mechanical,

and surface properties. In addition to experimental work, they developed a fiber simulation model which helped them to explain the partial relationships exist between the fiber dimensional properties and its frictional characteristics.

As previously mentioned, fiber crimp affects overall frictional properties of fiber assemblies. Lewin et al. compared the crimp behavior of two cotton varieties: Deltapine 15 and Acala 1517 [86,87]. They measured both the geometrical waviness of fibers and the specific energy required to remove the crimp from them. They concluded that Deltapine fibers were more significantly crimped at the 1% level of confidence. They also measured the force required to separate a fiber from the lot. The results showed that Deltapine fibers were more entangled since the force required to separate them was significantly higher on average. Alexander et al. studied the crimp recovery of the same cotton varieties [88–90]. They reported that the crimp recovery of fibers after multiple extension cycles consisted of both the immediate elastic recovery part and the irreversible part. Their results showed that the amount of the stable part of cotton crimp varies significantly between varieties. While the Deltapine fibers recovered about 50 percent of their initial crimp after extension and relaxation, the Acala variety fibers recovered only 25 percent of their initial crimp.

The influence of the surface topography on the mechanical interlocking between cotton fibers and a metallic surface was studied [77]. The mechanical interlocking took place in both directions when the ratio between the height of surface asperities on the metallic surface,  $h$ , and the radius of cotton fiber,  $r$ , exceeded one. However, the mechanical interlocking occurred in only one direction when the ratio  $h/r$  was slightly less than one. According to this paper, no mechanical interlocking took place when the ratio  $h/r$  was reduced to the lower values. This study shows the importance of surface topography on sliding friction experiments of cotton fiber assemblies.

Macroscale friction largely depends on the physical properties and environmental conditions of the counter faces during relative motion. Since real surfaces are rough, macroscale friction always involves the complex interactions between the multi-asperity contacts of both contacting surfaces on length scales ranging from molecular to macroscopic. Quantifying the number of asperities in contact and monitoring their deformation are difficult to achieve in practice. For these reasons, macroscale friction results are often unclear and may not be the best tool for fundamental research on interfacial forces and friction. The next sections provide a literature review on the subject of single asperity contact experiments on polymeric and biological substrates.

### 3. Nanoscale Friction and Adhesion

#### 3.1. Nanoscale Friction on Viscoelastic Surfaces

During the last two decades, the invention of surface force apparatuses (SFAs) [91] and atomic force microscope (AFM) [92] marked a big step forward in measuring real contact area and frictional forces at the nanoscale [93–98]. A systematic friction experiments at the nanoscale (nanotribology) avoids the complexity of multi-asperity contact interactions. This new area of study has led to the fundamental understanding of friction forces at the molecular level [57,99,100].

The AFM has been widely used to measure interfacial frictional forces between a probe tip and a surface. The design of the AFM has been reviewed extensively elsewhere (Figure 5a–c) [93–95,97,99]. Briefly, the AFM probe consists of a sharp tip (radius of curvature varies between ~8 and 500 nm) attached to a cantilever with a low spring constant. Rectangular cantilevers are typically 225  $\mu\text{m}$  long and 35  $\mu\text{m}$  wide. In the contact mode AFM, as the tip approaches a sample surface, it raster scans the surface, using a piezoelectric scanner. Based on the stiffness of the cantilever, scanning can be performed under a range of normal loads from nano- to micronewtons. In the case of nominally flat surfaces, the friction force between the surface and the tip during sliding is the only cause of the lateral torsion (or twist) of the cantilever. The cantilever torsion deflection is on the order of several mrad and is precisely monitored by reflecting a laser beam off the back of the cantilever and a position-sensitive photo-detector (PSPD) sensor. Therefore, the lateral deflection of the cantilever, with respect to the

plane of the sample surface, produces a signal corresponding to the interfacial friction between the tip and the surface. In order to convert this torsion signal to the absolute friction force, one should first measure the lateral torsional sensitivity of the cantilever. Absolute friction force between the AFM tip and a given surface can be determined with the following equation:

$$F_f = \Delta V \times S \times k_t \quad (17)$$

where  $\Delta V$  is the torsional signal difference (obtained from trace and retrace scanning directions) in volts,  $S$  is the cantilever torsional sensitivity in volts/meter, and  $k_t$  is the cantilever torsional spring constant in newtons/meter. Determining the cantilever torsional sensitivity is a difficult and time-consuming task. Meanwhile, the torsion signal is still being reported in most scientific publications as an indication of friction forces between the AFM tip and a surface. In the case of comparative studies between different materials, it is recommended that the same AFM tip to be used for all measurements. This practice reduces the variability that may arise due to the variation in cantilever sensitivity and tip radius of curvature.

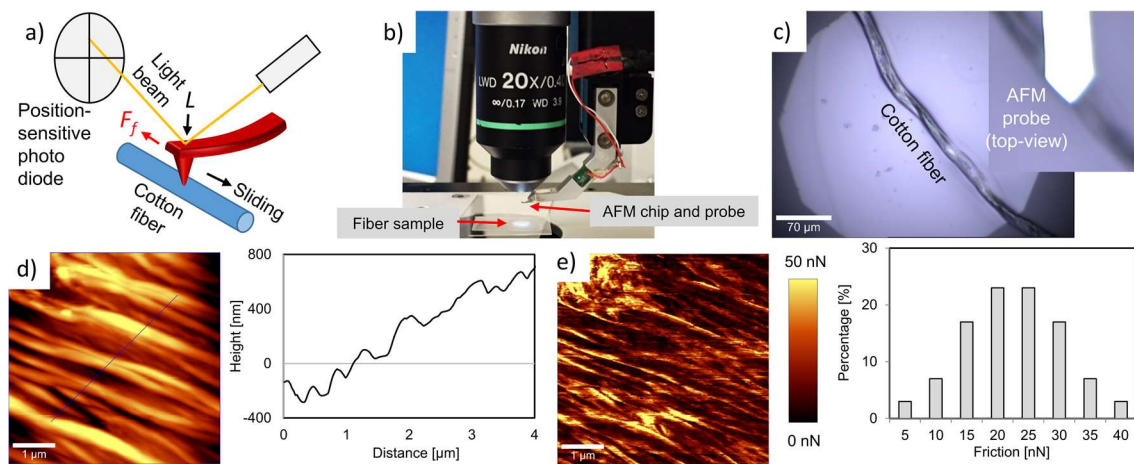


**Figure 5.** (a) Schematic of an atomic force microscope (AFM) probe as it raster scans the fiber surface; (b) AFM chip mounted on AFM head which is coupled with optical microscope system; (c) cotton fiber and AFM cantilever viewed from optical microscope; (d) typical topography image of cotton fiber surface. The plot show profile of fiber surface along the line; (e) corresponding friction image of the fiber surface. Plot shows the distribution of friction force.

During the AFM contact mode imaging of a surface (Figure 5d), the process of raster scanning a surface produces a high-resolution image of the spatial distribution of interfacial friction (Figure 5e). This approach is known as lateral force microscopy (LFM) or friction force microscopy (FFM). The nanotribological properties of nominally flat surfaces such as silicon-based materials, gold, diamond, sapphire, mica, graphene, and atomically thin lamellar materials have been extensively studied. The AFM experiments along with molecular dynamic simulations on these well-defined surfaces have improved our understanding of the influence of various physical phenomena, such as surface roughness, stick-slip behavior, wear, and asperity interlocking, on friction [95–97,99,100]. The nanotribological, wear, and stability properties of smooth surfaces coated with Langmuir-Blodgett monolayers and thin organic lubricant films have been also investigated [101,102]. The AFM results on self-assembled monolayers have shown that packing density, layer thickness, chain length, and chemistry of constituent molecules significantly affect the friction of coated surface.

Several studies have been conducted to measure the nanoscale frictional properties of rough polymeric surfaces and study their relationships with local rheological parameters [103–108]. In the case of rough surfaces, not only the friction forces between the AFM tip and the surface, but also the local slopes of the surface, and the plowing of the soft surfaces during sliding can cause a lateral

torsion of the cantilever. However, in most cases, the shear stress between the tip and the surface still has a major effect on the cantilever torsion. For polymers, generally speaking, single asperity frictional forces are largely influenced by the extent of their internal molecular relaxation, which manifests itself in viscoelastic energy dissipative characteristics of the polymer. Here, some applications of the AFM only in the study of polymer surfaces nanotribology will be reviewed.

Nanoscale friction measurements can be used to study the surface structure and molecular conformation of polymer crystals. Nisman et al. measured surface frictional forces on single lamellar crystals of poly(oxymethylene) (POM) [109]. The results showed that the magnitude of frictional forces changed depending on the direction of AFM scanning. This observation revealed an anisotropic nature of friction at the surface of different folded domains of single POM crystals. The anisotropic effect was attributed to the presence of directionally ordered chain folds and chain loops at the surface of different folded domains.

Interrelationships between materials surface characteristics can be investigated using AFM. Bhushan et al. measured nanoscale friction of PET films and investigated its relationship with surface roughness, stiffness, and macroscopic friction values [110]. Their results showed a lower coefficient of friction for nanofriction than macroscopic friction, mainly because of a lesser plowing effect with nanoscale single asperity friction measurements. Cho et al. measured nano- and macroscale frictional properties of PET, PP, and HDPE films [111]. Their results are in agreement with previous studies, reporting lower values for friction at nanoscale compared to macroscale. Kumar et al. studied the effect of adding TiO<sub>2</sub> nanoparticles on nanotribological properties of high density PE (HDPE), linear low density PE (LLDPE), and low density PE (LDPE) polymer blends [112]. The resulting nanocomposite films exhibited higher stiffness and a lower nanoscale friction coefficient. Tambe et al. studied the scale dependence of friction on polymer surfaces [113]. They measured friction over 2 μm to 25 μm length scales and reported lower coefficient of friction at smaller length scales. They reported that friction is highly influenced by the surface roughness of contacting bodies and its scale dependence originates from the variation in the surface roughness over different length scales.

Bogdanovic et al. mounted a cellulose colloidal microsphere, with an approximate diameter of 30–50 μm, to the tip of an AFM cantilever [114]. This technique allowed them to quantify the interfacial friction for a cellulose microsphere sliding against silica and chemically modified silica surfaces. Using both the Derjaguin–Muller–Toporov (DMT) and linear fits, they showed that the magnitude of frictional force is higher for the bare silica surface, which is more hydrophilic, compared to the hydrophobic methylated silica. The variation in friction between the two surfaces was attributed to the differences in their surface chemistry. The existence of polar groups and the ability of the surface to create a water meniscus around the microsphere tip were stated to be two important factors that influenced the friction. Nordgren et al. used the same approach to measure friction between untreated and chitosan treated cellulose microspheres at different pH values [115]. Their results demonstrated that the biolubrication properties of the chitosan layer were significantly increased at lower pH—mainly due to its high surface charges in low pH values.

Morphological and nanotribological properties of different components of thin gelatin films have been investigated [116]. The plot of frictional force versus applied load, along with the AFM force–distance data, showed that a thin gelatin is composed of two structurally different regions: a “first layer” of continuous high-friction and low-stiffness film; and a “second layer” of low-friction and high-stiffness islands. It was stated that cross-linking and intramolecular folding of the gelatin chains constrained the molecular relaxational freedom and reduced the viscoelastic dissipation characteristics of the polymer network, resulting in lower single asperity frictional properties and stiffer substrate.

Repeated raster scanning at nonperturbative normal force and high velocities gradually elevates the temperature of the scanning region. A cumulative effect of friction-derived heating substantially increases the frictional forces of the substrate until it reaches a dynamic equilibrium. The role of frictional heating on phase transformation of crystalline and semicrystalline components of a gelatin film has been studied [117]. It was shown that a crystalline polymer tends to transform directly from

glassy state to melted under nonperturbative frictional heating, while the semicrystalline polymer first passed through a rubbery phase before melting. Resting the polymer film at room temperature allowed the frictional heated region to relax toward the ground state.

Scan-velocity dependency of frictional forces on gelatin films have been investigated [108,117]. Velocity dependency of friction seemed to be well-correlated to the different molecular relaxation peaks of a tangent delta plot (tangent delta indicates the relative contribution of viscous and elastic properties to the viscoelastic moduli of a material in dynamic mechanical analysis (DMA) experiments as a function of time and temperature). While the tests were performed in decreasing scan velocity order, the larger friction force in very high scan velocities ( $>300 \mu\text{m/s}$ ) was assigned to the secondary molecular conformation peak ( $\beta$  relaxation process) in the tangent delta plot. An increase in frictional force at lower scan velocities ( $<100 \mu\text{m/s}$ ) was attributed to the glass transition peak ( $\alpha$  relaxation process). A similar type of research has been performed to investigate the velocity dependency of frictional forces as a function of molecular weight on monodisperse and polydisperse polystyrene (PS) films [118,119]. The results are in agreement with previous studies; that is, magnitude of friction is proportional to the loss modulus of the polymer, which itself depends on the glassy or rubbery state of the polymer.

In order to further investigate the causation of frictional energy dissipation processes in polymeric surfaces, the velocity dependency of frictional forces on different polymer films such as poly(vinyl alcohol) (PVA), crystalline poly(ethylene terephthalate) (PET), and poly(vinyl acetate) (PVAc) have been tested [120]. A comparison between PET viscoelastic loss modulus and its AFM friction results indicated that the variation in frictional forces at high scan velocities is similar to the  $\beta$  relaxation process at high frequencies. For all other polymers used in the research, it was shown that changes in the  $\alpha$  and/or  $\beta$  relaxation behaviors as a function of temperature, water content, or plasticizing have comparable effects on the velocity dependency of frictional response. Temperature dependency of frictional forces on poly(methyl methacrylate) (PMMA) and PS thin films has also been studied [121]. In this study, frictional forces at different temperatures and the corresponding tangent delta values were compared. The results revealed a good correlation between temperature-dependent changes in friction and the molecular relaxation peaks as measured by DMA. Both for PMMA and PS, frictional forces increased significantly near the glass transition temperature, due to the variation in viscoelastic loss near this temperature. Time-temperature superposition of friction on a PMMA surface has also been studied [122]. Using a temperature-controlled AFM, authors were able to perform friction tests at different velocities for various temperatures. They constructed a master curve of frictional forces and showed that the  $\beta$  relaxation process shifts to the lower temperatures with decreasing the sliding velocity.

The AFM friction and wear measurements can be used to study the interfacial adhesive forces relevant to different components of nanocomposite and layered materials [123]. Using this technique, the cohesive strength and the detachment process of extracellular polymeric biofilms have been studied. Authors applied successive AFM friction tests at high contact force (50 nN) to abrasively shear and remove the biofilm from a mica surface. After calibration of friction force and conversion of the raw friction signal (volts) to the friction force (nN), they were able to develop an AFM based method to determine the cohesive energy of a volume of biofilm in units of  $\text{nJ}/\mu\text{m}^3$ . In another study, authors applied the same methodology on various nanocomposites and probed the bonding strength between PET matrix and different nanofillers such as graphene or clay platelet [124].

Fundamental experiments on the interfacial friction mechanism of polymer-on-polymer surfaces have been conducted with SFA [56,57,125–127]. These studies showed that the polymer interfacial friction depends on the arrangement and state of macromolecule chains at, or very near, the surfaces. During sliding friction, polymer segments, in the forms of chain loops and free-ends, penetrate into the opposite surface and cause an increase in both the shear angle and the number of van der Waals bonds between the surfaces. It has been reported that changes in the degree of crosslinking or the density of free-ends (chain scission) at the polymer surface significantly affect interfacial polymer-on-polymer

friction. In fact, cross-linking of glassy polystyrene (PS) and poly(vinylbenzyl chloride) (PVBC) resulted in lower interfacial friction. This effect was attributed to the reduced density of the polymer segments at the surfaces. As a result of crosslinking, the polymer network becomes more rigid and polymer free-ends might not be able to interpenetrate into the opposing surface. On the other hand, scission (bond-breaking) of the cross-linked PS and PVBC surfaces increased the interfacial friction force considerably. In this scenario, free-ends penetrate deeply into the opposing surface while they are still anchored to their own surface. According to these studies, it can be concluded that interfacial friction force between polymer surfaces depends on the number of chain ends at the surface, the rate of interpenetration of polymer segments, and the extent of the penetration. In addition to these factors, one should also consider the effects of the real contact area and the asperity deformation in analyzing the overall friction mechanism between macroscopic polymeric contact systems. It is reported that the polymer-on-polymer friction mechanism for a single asperity junction can be applied to multiple asperity contacts by implementing proper statistical averaging and summing techniques.

### 3.2. Nanoscale Adhesion on Viscoelastic Surfaces

Various nanomechanical attributes of surfaces—such as elastic modulus, plasticity, and adhesion—can be measured by quantifying forces acting on the AFM tip as it vertically approaches a surface, slightly indents it, and finally is withdrawn from it [128,129]. This technique has been extensively applied to quantify the surface nanomechanical properties of silicone and polymeric thin films, SAMs, nanocomposite materials, and living cells [128,130–134]. Nanomechanical properties of plant cell walls have been also investigated [135–137]. These studies have provided invaluable insight into the understanding of plant cell growth and development (morphogenesis). In the research reported herein, part of the focus will be on the nanoscale adhesive forces between an AFM tip and the cotton fiber surface, mainly due to the critical contribution of adhesion on the overall frictional responses of the specimen. As mentioned earlier, the correlation between adhesion hysteresis and friction for polymers has been well-studied [57,126]. Additionally, variation in surface adhesion properties has been previously utilized to discriminate between different materials.

Adhesive forces between two surfaces can be extracted from a plot of interfacial forces between the surfaces versus their separation distance, commonly known as a force–distance curve (FDC). Specifically, in the AFM technique, the FDC is obtained from measuring the vertical deflection of a cantilever (which can be converted to unit force) as a function of piezoelectric tube vertical extension (which can be converted to indentation/separation distance) when the tip is brought into contact with the sample and then withdrawn. Similar to microscale friction, the main advantage of adhesion measurements with AFM is the single asperity contact at the molecular level, which removes the ambiguity due to multiple asperity contacts. A hypothetical FDC and its different regions are shown in Figure 6. The general shape of the FDC resembles a typical nonbonding intermolecular force curve between two nonpolar particles. In region A, the tip is in resting position and the net force acting on it is zero. In region B, as the tip is driven toward the surface, at some critical distance, the forces acting on the tip suddenly become attractive, and the tip jumps to contact. In order to accommodate the abrupt movement of the tip, the cantilever experiences an instability and bends forward. By multiplying the vertical deflection of the cantilever in nm with its spring constant in N/m, total forces acting on the tip can be quantified. This sudden large attractive force acting on the tip is defined as the pull-on (or snap-in) force and its magnitude can be explained by extent of ever-present van der Waals, electrostatic, capillary, and chemical bonding forces. In region C, as the piezoelectric tube continues to extend toward the sample surface, the repulsive forces are first detected and the net force starts to increase. This point is defined as the tip-surface contact point. After this point, the tip starts to penetrate into the sample and causes elastic and/or plastic deformation of the surface (assuming higher stiffness value for the tip). Meanwhile, the cantilever deflection gradually changes from being bent downward to upward. The indentation process continues until ultimate contact is reached at a predefined maximum upward deflection. In region D, the piezoelement movement reverses and it

begins to withdraw the tip. When the tip is being retracted, it still remains in contact with the surface until the cantilever exerts sufficient tensile force to overcome the adhesive bonds formed between the tip and the surface (pull-off force). The difference between the pull-off force and the forces acting on the tip at the resting position is proportional to the adhesion force, which is significantly affected by real contact area and chemistry of the two materials. Upon the tip–sample separation (snap-out), depending on its spring constant, the cantilever experiences a second instability and springs back to the resting position in region E.

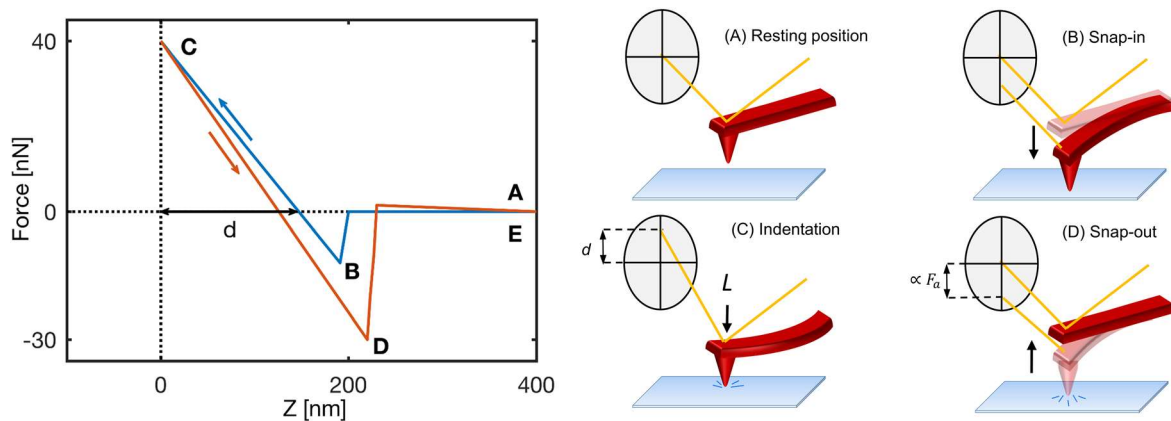


**Figure 6.** Hypothetical force–distance curve and its different regions: Resting position, snapping in (or jump-into-contact), indentation, and snapping out (or pull-off).

There are three modes of deformation associated with the force measurement technique with the AFM: the cantilever is either bent upward, or downward, or twisted. These cantilever deformations are associated with surface stiffness, adhesion, and friction, respectively. The deformation can be converted to the forces causing it with Hooke’s law. That is, the strain (deformation) of an elastic material is proportional to the stress  $F_c$  applied to it:

$$F = k_c d_c \tag{18}$$

Here,  $k_c$  is the spring constant of the cantilever, and  $d_c$  is the deflection of the cantilever. By obtaining forces acting on the cantilever, the force–distance curve of a given material’s surface can be acquired (the distance is obtained by adding the piezoelectric motion to  $d_c$ ). Therefore, the force of adhesion, the stiffness of the surface, and the friction between tip and surface can be extracted from the curve. Since the invention of the AFM, one of the main challenges has been how to precisely measure the deflection of the cantilever,  $d_c$ , as the main output signal of the AFM instrument. In almost all the AFMs available on the market, the deflection of the cantilever is measured with the optical lever technique. In this method, a beam from a diode is adjusted onto the cantilever and reflects from its shiny end. A PSD monitors the position of the reflected beam. As the cantilever bends, the reflection angle of the beam changes to twice the change of the slope at the end of the cantilever. Therefore, the deflection of the cantilever can be measured as [128]:

$$F \propto d_c = \frac{Fl^3}{3EI} = \frac{\Delta_{PSD}l}{3b} \tag{19}$$

Here,  $l$  is the length of the cantilever,  $I$  is the moment of inertia of the cantilever,  $E$  is the Young’s modulus of the cantilever,  $F$  is the force acting on the cantilever,  $\Delta_{PSD}$  is the distance the laser spot moves on the PSD, and  $b$  is the distance between the PSD and the end of the cantilever. In the optical lever technique, the  $\Delta_{PSD}$  is the only output of the instrument. This output is used to calculate  $d_c$ , the deflection of the cantilever, the variable of interest. Improper adjustment of the light beam on a PSD while the cantilever is in the resting position can be an important source of error in measuring

surface forces. Two other sources of error in using AFM include the possibility of contaminating the tip during scanning and lack of standard procedure to examine the true radius of curvature of the tip before performing nanomechanical testing.

Different aspects of the adhesive force measurement technique with the AFM have been reviewed and studied. Batteas et al. studied the adhesion and wear of colloidal silica nanoparticles at different pH values. In order to simulate the actual particle-particle interaction, they used AFM probes with a blunt tip (curvature radius of ~50 nm). They showed that the tip-particle adhesion, as measured by the JKR contact mechanics, is higher at low pH values [138]. Burnham et al. attempted to model the magnitude of attractive forces between the tip and surface using magnetic, electrostatic, and van der Waals interactions [129]. For uncharged and nonmagnetic surfaces, they concluded that the effect of van der Waals forces on the tip is often masked by the longer-range attractive forces which are better explained by capillary, fixed dipole, and patch charge models. Kawai et al. measured the pull-on and pull-off forces for eight reference surfaces [139]. They showed that the pull-off forces were well-correlated with the adhesion energy of the reference samples as measured from contact angle experiments. Mate et al. utilized the shape of the pull-on region of the FDC to estimate the thickness of the ultrathin polymeric liquid films (less than ~300 Å thick) on a flat silicon surface [140,141]. Using this technique, they were able to map the spatial distribution of the film thickness coated on the surface. Bhushan et al. performed an adhesive force measurement study on the 2-nm thick lubricant layer film [142]. They concluded that the magnitude of meniscus forces between the tip and the lubricant layer, which manifested themselves in the corresponding pull-off force, was proportional to the film thickness. The dependence of adhesion on both surface topography and nanomechanics has been widely investigated. Mizes et al. demonstrated that the local curvature of the surface affects the adhesion between the AFM tip and the surface [143]. This observation was explained by the fact that a real contact area was much lower for contacts in the apex of an asperity compared to that of in the bottom of a pit. Sirghi et al. modeled the capillary and interfacial tension forces between an AFM tip and a substrate based on the local radius of curvature of the asperity (positive value for a convex curvature, and negative for a concave curvature) [144]. Their analytical solution demonstrated that the capillary forces were much larger for concave surface curvature. Eaton et al. investigated the capability of the adhesive force measurement technique to discriminate between different domains of polymer blends based on their surface energetic and nanoscale stiffness [145]. The adhesive force measurement results on PDDMA/PMMA thin films demonstrated that the average force of adhesion was much higher for PDDMA-rich domain compared to PMMA regions, mainly due to its higher surface deformation and, consequently, greater tip-sample real contact area [146,147]. Begat et al. glued pharmaceutical micro-particles from various inhaler formulations to a tipless cantilever and measured the adhesive forces between them and a reference substrate with well-defined surface texture [148]. Using this technique, they were able to quantify the inter-particle cohesive-adhesive forces and predict the bulk properties of the bulk powder formulation.

A positive strong correlation exists between the adhesion hysteresis and frictional forces [57,126,127]. Adhesion hysteresis is defined as the difference between the work needed to separate two surfaces (unloading) and that originally gained on bringing them together (loading) [149–151]. Tirrell investigated the adhesion hysteresis of various polymeric materials [151]. For hysteretic surfaces, such as polymers, the effect is attributed to both the reorientation of molecules near the surface and the viscoelasticity of the bulk material. Since a certain level of molecular rearrangement and transformation may take place after contact is made, only the loading data can be fit to the JKR model for the analysis of real contact area. The contact formation during loading is governed by the chemical constituents of the contacting materials.

Appropriate selection of an AFM probe is a crucial task for successful nanoscale adhesion and friction experiments. Generally, there are two important probe parameters which restrain the magnitude of the applied pressure to the surface: cantilever stiffness and tip apex radius. Cantilevers with low spring constant are more efficient in the study of adhesive properties of soft materials, since the

pull-off deflection is higher for flexible cantilevers. Stiff cantilevers, on the other hand, are mostly used for indentation purposes. With regards to the radius of curvature of the tip, large radius tip probes are more favorable than sharp tip probes in the study of polymeric and biological substrates. The larger contact area for these tips provides the following advantages: (i) the total interaction force between the tip and the surface is higher; as a result, the sensitivity to adhesion and friction forces is maximized; (ii) The applied pressure is lower; therefore, the penetration depth will be limited to a few nanometers; (iii) The stress concentration in front of the tip is lower, which reduces the plastic deformation and surface damage in testing of compliant thin films; (iv) The probability of non-normal indentation is minimized since the local friction between the tip and the surface is enhanced (the indentation process occurs approximately perpendicular to the surface); (v) Finally, the spherical shape of the apex of the tip simplifies the implementation of the contact mechanics analysis.

Successive measurements of FDCs across the specimen surface can be used to generate a map of local adhesion, where each pixel represents a magnitude of the tip–sample adhesion force of that area [152]. Lately, a new FDC mapping technique has been commercialized, known as pulsed-force microscopy, with the capability to produce high-resolution topography and nanomechanical properties images simultaneously [153,154]. With this method (commercially known as the peak force tapping mode), as the z-piezoelement raster scans the surface, it also resonates at very high frequencies. During each resonance cycle, the tip engages the surface and then is retraced from it at a given amplitude; thereby, hundreds of FDCs can be produced in matter of milliseconds [155,156]. This AFM mode has gained increased popularity in the field of surface characterization of biological materials [157,158]. With the sinusoidal modulation of the z-piezoelement, small normal forces can be applied more precisely compared to conventional force volume mode.

### 3.3. Nanomechanical Properties of Plant Tissues

The plant cells are covered with a thin extracellular membrane, known as the cuticle, which strengthens the overall structural stability of the cell and preserves its physiological integrity [159–161]. In the study of plant cell morphogenesis, precise measurements of the nanoscale mechanical properties of plant cell surfaces are crucial for investigations on the role of cuticle biomechanics in a cell shape changes and growth rate [135,162]. The cuticle thickness varies significantly between different plant organs and species and also during cell development. This plant cell outer layer is a hydrophobic multicomponent structure and mainly consists of the biopolyester cutin, various lipid-derived compounds or so-called waxes, and pectins. Cutin is an insoluble biopolymer network makes up of  $C_{16}$  and  $C_{18}$  fatty acid monomers cross-linked by ester bonds. Cutin encompasses 40–80% weight of the cuticle and can be submicron to 10  $\mu\text{m}$  thick. Cuticular waxes are chiefly composed of n-acyl alkane derivatives with chain length of  $C_{20}$  to  $C_{40}$ . Plant cell waxy components mostly travel through different layers of the cuticular membrane and build up on the outermost layer of the cuticle. After deposition on a plant organ surface, they self-assemble into a thin continuous lipid-film. They form various crystalline microstructures, such as tubules (0.3 – 3  $\mu\text{m}$  long and 0.1 – 0.3  $\mu\text{m}$  wide), platelets, and rodlets. Cuticular waxes directly affect interfacial bioprocesses and environmental interactions of plant organs. Self-assembly and growth of wax crystals has been monitored with AFM time-series images [163]. These observations showed that the morphology of wax crystals depends on the growth conditions, such as temperature and moisture content, the chemical composition of lipid compounds, and the structural template effect of the underlying substrate. Pectin polysaccharides can also be found in the outer surface of the cuticle. Round et al. studied the structure of individual pectin macromolecules extracted from green tomato fruits, using the AFM [164,165]. Their work demonstrated the capabilities of AFM images in revealing molecular weight, length, branching, and aggregation of individual pectin polymers.

Even with recent advances in AFM techniques, quantifying the local nanomechanical attributes of soft biological materials is a challenging subject. Often, due to the natural surface roughness and viscoelasticity of biological materials, accurate measurements of surface nanomechanical properties

require an implementation of sophisticated contact mechanics models. Studies have been conducted to examine the surface biophysical behavior of cutin films, isolated from the cuticle of tomato fruits, with AFM [137,166,167]. Round et al. studied the effect of moisture content on the rheology of such films [167]. They reported that the surface elastic modulus, as obtained by fitting the FDCs with the Hertz model, decreases with increasing water absorption in a highly nonlinear fashion. They concluded that the cutin film has a rubbery characteristic and water molecules increase its polymer chain mobility. Bhushan et al. investigated nanoscale friction of four different plant leaves in dried state: *lotus*, *colocasia*, *fagus*, and *magnolia* [168]. According to the results, the hydrophilic leaves (*fagus*, and *magnolia*) showed a higher friction coefficient than the hydrophobic ones (*lotus* and *colocasia*). For hydrophilic surfaces, the contact area is higher due to the formation of water meniscus between the tip and the surface.

### 3.4. Nanofrictional and Nanomechanical Properties of Cotton Fibers

A fully developed cotton fiber is composed of five different layers: the cuticle, the primary cell wall, the winding layer, the secondary cell wall, and the cell lumen [169]. The cotton fiber cuticle is mostly made of lipids, alcohols, and fatty acids. These compounds are collectively called “cotton waxes” [170]. The cotton fiber cuticle also contains some portion of pectins [171]. Due to the presence of waxes and pectins in the cuticle, untreated native cotton fibers are hydrophobic [170]. The waxy layer is about 200 to 300 nm thick [169]. Cotton fiber wax content varies significantly among different varieties. Various studies have reported a strong positive relationship between cotton fibers wax content and their surface area [73,74,172–174]. El Mogahzy showed that the frictional properties of cotton fibers are influenced by their wax content [73].

Very few studies have been published on nano- and microscale friction of cotton fibers. Zhang et al. investigated nanoscale frictional properties of cotton fibers [76]. The nanofrictional characterization of textile fibers can be used to evaluate the performance of chemical treatments and fiber surface modification techniques. The authors showed that the nanoscale friction coefficient increased after multiple washes in the absence of fabric conditioner. They concluded that excessive washing cycles damages the fiber surface and increases the fiber surface roughness, leading to higher friction forces between the AFM probe and fiber surface. In the presence of fabric conditioner, however, the friction coefficient decreased. Their results indicate that the nanoscale friction forces obey Amontons’ law of friction. In a recent study, Hosseianli et al. have compared the surface nanofrictional and nanomechanical properties of two different varieties of cotton fibers [79]. The varieties were tested in their study were shown to exhibit significantly different macroscale frictional properties. Their results indicated that fibers with higher macroscale friction were also associated with higher nanoscale friction, adhesion, and deformation. They hypothesized that differences in surface nanomechanical properties of these fibers might be due to fiber surface hydrophobicity and stiffness, which in turn may depend on the waxy layer thickness, fatty acids hydrocarbon chain length, and film viscosity. Other studies in application of AFM to characterize cotton fibers were limited to investigating the topography of both the surface and the cross-section of fibers at the nanoscale [72,175–177]. These studies obtained high-resolution AFM images of cotton fibers in tapping mode to study the geometry of cellulose microfibrils embedded inside the internal structure of fibers.

## 4. Future Research

At the macroscale, experiments have been designed to investigate the correlations between the fiber processing efficiency (in terms of fiber breakage and foreign particle removal in lint cleaner or carding) and the fiber friction. The fiber friction itself can be treated as a dependent variable, which is affected by the fiber wax content, the waxy layer thickness, and the fatty acids hydrocarbon chain length. In these experiments, the amount of fiber in samples needs to be controlled either by weight or by the total number of fibers in contact with another surface.

At the nanoscale, the future research can focus on the origin of attractive and adhesive force between cotton fiber surface (the cuticle) and an AFM tip. As previously discussed, the nature of the

adhesion forces probed with the AFM is complex. The magnitude of the adhesion force depends on the topography of the surface, capillary forces, and surface energy characteristics of the tip and the surface. In the case of cotton fibers, it needs to be understood if there is any correlation between the magnitude of the adhesive force and the thickness of the waxy layer. Under one possible hypothetical scenario, as the AFM tip approaches the fiber surface, sudden contact is made with this lipid layer (Figure 6). As the tip further approaches the fiber surface, it may penetrate into the waxy layer until it reaches an ultimate depth of contact. As the tip is withdrawn from the surface, a pull-off force is needed to break the possible lipid meniscus between the tip and the fiber surface. Theoretically speaking, due to the hydrophobicity of the waxy and pectin compounds on the fiber surface, the formation of the water meniscus is not likely in AFM adhesion experiments. Therefore, it needs to be examined if there is any correlation between the force required to break the lipid meniscus and the thickness of the lipid layer on the fiber surface.

**Author Contributions:** F.H. conducted the survey and wrote the manuscript. J.A.T. supervised the project, guided the research, and edited the final manuscript.

**Funding:** This work was supported in part by the Cotton Incorporated under Grant 05-755. This work was supported in part by Alex Thomasson of the Department of Biological and Agricultural Engineering at Texas A&M University.

**Conflicts of Interest:** The authors declare no conflicts of interest.

## References

1. Anthony, W.S.; Mayfield, W.D. *Cotton Ginners Handbook*; United States Department of Agriculture, Agricultural Research Service: Beltsville, MD, USA, 1994; ISBN 0160453690.
2. Thomasson, J.A.; Shearer, S.A. Correlation of NIR data with cotton quality characteristics. *Trans. ASAE* **1995**, *38*, 1005–1010. [[CrossRef](#)]
3. Sui, R.; Thomasson, J.A.; Ge, Y.; Morgan, C. Multispectral Sensor for In-Situ Cotton Fiber Quality Measurement. *Trans. ASABE* **2008**, *51*, 2201–2208. [[CrossRef](#)]
4. Shahriar, M.; Scott-Fleming, I.; Sari-Sarraf, H.; Hequet, E. A machine vision system to estimate cotton fiber maturity from longitudinal view using a transfer learning approach. *Mach. Vis. Appl.* **2013**, *24*, 1661–1683. [[CrossRef](#)]
5. Griffin, A.C.; Moore, V.P. Relation of Physical Properties of Cotton to Commerce and Ginning Research. *Trans. ASAE* **1965**, *8*, 488–490. [[CrossRef](#)]
6. Stedronsky, V.L. Ginning Processes and Their Effects on Cotton Quality. *Trans. ASAE* **1966**, *9*, 282–283. [[CrossRef](#)]
7. Childers, R.E.; Baker, R.V. Effect of Moisture Conditioning on Ginning Performance and Fiber Quality of High Plains Cotton. *Trans. ASAE* **1978**, *21*, 379–384. [[CrossRef](#)]
8. Anthony, W.S.; Bragg, C.K. Response of Cotton Fiber Length Distribution to Production and Ginning Practices. *Trans. ASAE* **1987**, *30*, 290–296. [[CrossRef](#)]
9. Anthony, W.S. Cotton Length Uniformity and Short Fiber Content. *Trans. ASAE* **1992**, *35*, 443–449. [[CrossRef](#)]
10. Anthony, W.S. Impact of Cotton Gin Machinery Sequences on Fiber Value and Quality. *Appl. Eng. Agric.* **1996**, *12*, 351–363. [[CrossRef](#)]
11. Hosseinali, F. Investigation on the Tensile Properties of Individual Cotton (*Gossypium hirsutum* L.) Fibers. M.S. Thesis, Texas Tech University, Lubbock, TX, USA, 2012.
12. Mangialardi, G.J. Lint Cleaning at Cotton Gins. *Cott. Gin Oil Mill Press* **1988**, *89*, 8.
13. Hughs, S.E.; Armijo, C.B.; Foulk, J.A. Upland fiber changes due to ginning and lint cleaning. *J. Cotton Sci.* **2013**, *17*, 115–124.
14. Sui, R.; Thomasson, J.A.; Byler, R.K.; Boykin, J.C.; Barnes, E.M. Effect of machine-fiber interaction on cotton fiber quality and foreign-matter particle attachment to fiber. *J. Cotton Sci.* **2010**, *153*, 145–153.
15. Anthony, W.S.; Columbus, E.P. Principles of Dust Removal in Gin Machinery: Theoretical and Measured. *J. Eng. Ind.* **1985**, *107*, 288. [[CrossRef](#)]
16. Columbus, E.P. Principle Forces Applied to Fine Dust in Lint Cleaners. *Trans. ASAE* **1985**, *28*, 2042–2046. [[CrossRef](#)]

17. Barker, G.L.; Baker, R.V. Prediction of Cotton Quality as a Function of Lint Cleaner Operating Parameters. *Trans. ASAE* **1986**, *29*, 702–706. [[CrossRef](#)]
18. Baker, R.V. Performance Characteristics of Saw-Type Lint Cleaners. *Trans. ASAE* **1978**, *21*, 1081–1087. [[CrossRef](#)]
19. Baker, R.V.; Towery, J.D.; Cocke, J.B. Effects of Lint-Cleaner Combing Ratio and Suction Nozzles on Cotton Dust Levels in Processing. *Text. Res. J.* **1981**, *51*, 497–502. [[CrossRef](#)]
20. Leonard, C.G.; Wright, T.E.; Hughs, S.E. Lint Cotton Cleaners with Notched Grid Bars. *Trans. ASAE* **1982**, *25*, 204–209. [[CrossRef](#)]
21. Columbus, E.P. Effect of Lint Cleaner Saw Speed and Tooth Density on Cotton Quality. *Trans. ASAE* **1985**, *28*, 1692–1696. [[CrossRef](#)]
22. Baker, R.V.; Brashears, A.D. Effects of Grid and Saw Variables on Lint Cleaner Performance. *Trans. ASAE* **1989**, *32*, 1138–1142. [[CrossRef](#)]
23. Mangialardi, G.J., Jr. Alternate Carding and Combing Procedures for Cotton Lint Cleaners. *Appl. Eng. Agric.* **1995**, *11*, 801–810. [[CrossRef](#)]
24. Le, S. Fiber Quality Properties Produced by Saw-Type Lint Cleaners. *Appl. Eng. Agric.* **2007**, *23*, 125–130. [[CrossRef](#)]
25. Gordon, S.G.; Bagshaw, K.M.; Horne, F.A. The Effect of Lint Cleaner Elements, Settings, and Fiber Moisture Content on Fiber Quality. *Trans. ASABE* **2011**, *54*, 2267–2278. [[CrossRef](#)]
26. Dever, J.K.; Gannaway, J.R.; Baker, R.V. Influence of cotton fiber strength and fineness on fiber damage during Lint cleaning. *Text. Res. J.* **1988**, *58*, 433–438. [[CrossRef](#)]
27. Mangialardi, G.J.; Lalor, W.F. Propensity of cotton varieties to neppiness. *Trans. ASAE* **1990**, *33*, 1748–1758. [[CrossRef](#)]
28. Hughs, S.E.; Lalor, W.F.; Wahba, F.T. Relationship of Ginning and Fiber Properties to Dyeing Imperfections. *Text. Res. J.* **1988**, *58*, 557–565. [[CrossRef](#)]
29. Israelachvili, J.N. *Intermolecular and Surface Forces*; Academic Press: Waltham, MA, USA, 1992; ISBN 0123751810.
30. Gao, J.; Luedtke, W.D.; Gourdon, D.; Ruths, M.; Israelachvili, J.N.; Landman, U. Frictional forces and Amontons' law: From the molecular to the macroscopic scale. *J. Phys. Chem. B* **2004**, *108*, 3410–3425. [[CrossRef](#)]
31. Homola, A.M.; Israelachvili, J.N.; McGuiggan, P.M.; Gee, M.L. Fundamental experimental studies in tribology: The transition from “interfacial” friction of undamaged molecularly smooth surfaces to “normal” friction with wear. *Wear* **1990**, *136*, 65–83. [[CrossRef](#)]
32. Tabor, D. Friction, Adhesion and Boundary Lubrication of Polymers. In *Advances in Polymer Friction and Wear*; Springer: Boston, MA, USA, 1974; pp. 5–30.
33. Lee, L.-H. Effect of Surface Energetics on Polymer Friction and Wear. In *Advances in Polymer Friction and Wear*; Springer: Boston, MA, USA, 1974; pp. 31–68.
34. Zeng, H. Adhesion and Friction Mechanisms of Polymer Surfaces and Thin Films. In *Polymer Adhesion, Friction, and Lubrication*; John Wiley & Sons, Inc.: Hoboken, NJ, USA, 2013; pp. 391–442; ISBN 9781118505175.
35. Sawyer, W.G.; Argibay, N.; Burris, D.L.; Krick, B.A. Mechanistic Studies in Friction and Wear of Bulk Materials. *Annu. Rev. Mater. Res.* **2014**, *44*, 395–427. [[CrossRef](#)]
36. Bahadur, S. The development of transfer layers and their role in polymer tribology. *Wear* **2000**, *245*, 92–99. [[CrossRef](#)]
37. Makinson, K.R.; Tabor, D. Friction and Transfer of Polytetrafluoroethylene. *Nature* **1964**, *201*, 464–466. [[CrossRef](#)]
38. Biswas, S.K.; Vijayan, K. Friction and wear of PTFE—A review. *Wear* **1992**, *158*, 193–211. [[CrossRef](#)]
39. Persson, B.N.J. Theory of rubber friction and contact mechanics. *J. Chem. Phys.* **2001**, *115*, 3840–3861. [[CrossRef](#)]
40. Nak-Ho, S.; Suh, N.P. Effect of fiber orientation on friction and wear of fiber reinforced polymeric composites. *Wear* **1979**, *53*, 129–141. [[CrossRef](#)]
41. Burris, D.L.; Sawyer, W.G. A low friction and ultra low wear rate PEEK/PTFE composite. *Wear* **2006**, *261*, 410–418. [[CrossRef](#)]
42. Bahadur, S.; Gong, D. The action of fillers in the modification of the tribological behavior of polymers. *Wear* **1992**, *158*, 41–59. [[CrossRef](#)]

43. Burris, D.L.; Boesl, B.; Bourne, G.R.; Sawyer, W.G. Polymeric Nanocomposites for Tribological Applications. *Macromol. Mater. Eng.* **2007**, *292*, 387–402. [[CrossRef](#)]
44. Gong, J.P.; Giasson, S.; Kampf, N.; Gohy, J.F.; Jerome, R.; Klein, J.; Gong, J.P. Friction and lubrication of hydrogels—Its richness and complexity. *Soft Matter* **2006**, *2*, 544–552. [[CrossRef](#)]
45. Landherr, L.J.T.; Cohen, C.; Agarwal, P.; Archer, L.A. Interfacial Friction and Adhesion of Polymer Brushes. *Langmuir* **2011**, *27*, 9387–9395. [[CrossRef](#)] [[PubMed](#)]
46. Lee, D.W.; Banquy, X.; Israelachvili, J.N. Stick-slip friction and wear of articular joints. *Proc. Natl. Acad. Sci. USA* **2013**, *110*, E567–E574. [[CrossRef](#)] [[PubMed](#)]
47. Yu, J.; Chary, S.; Das, S.; Tamelier, J.; Turner, K.L.; Israelachvili, J.N. Friction and Adhesion of Gecko-Inspired PDMS Flaps on Rough Surfaces. *Langmuir* **2012**, *28*, 11527–11534. [[CrossRef](#)] [[PubMed](#)]
48. Kang, T.; Banquy, X.; Heo, J.; Lim, C.; Lynd, N.A.; Lundberg, P.; Oh, D.X.; Lee, H.-K.; Hong, Y.-K.; Hwang, D.S.; et al. Mussel-Inspired Anchoring of Polymer Loops That Provide Superior Surface Lubrication and Antifouling Properties. *ACS Nano* **2016**, *10*, 930–937. [[CrossRef](#)] [[PubMed](#)]
49. Howell, H.G. The laws of static friction. *Text. Res. J.* **1953**, *23*, 589–591. [[CrossRef](#)]
50. Howell, H.G.; Mazur, J. Amontons' law and fibre friction. *J. Text. Inst. Trans.* **1953**, *44*, T59–T69. [[CrossRef](#)]
51. Howell, H.G. The laws of friction. *Nature* **1953**, *171*, 220. [[CrossRef](#)]
52. El Mogahzy, Y.E.; Gupta, B.S. Friction in fibrous materials. *Text. Res. J.* **1993**, *63*, 219–230. [[CrossRef](#)]
53. Gupta, B.S.; El Mogahzy, Y.E. Friction in Fibrous Materials: Part I: Structural Model. *Text. Res. J.* **1991**, *61*, 547–555. [[CrossRef](#)]
54. Lincoln, B. Frictional and Elastic Properties of High Polymeric Materials. *Br. J. Appl. Phys.* **1952**, *3*, 260–263. [[CrossRef](#)]
55. Archard, J.F. Elastic Deformation and the Laws of Friction. *Proc. R. Soc. A Math. Phys. Eng. Sci.* **1957**, *243*, 190–205. [[CrossRef](#)]
56. Urbakh, M.; Klafter, J.; Gourdon, D.; Israelachvili, J. The nonlinear nature of friction. *Nature* **2004**, *430*, 525–528. [[CrossRef](#)] [[PubMed](#)]
57. Maeda, N.; Chen, N.; Tirrell, M.; Israelachvili, J.N. Adhesion and friction mechanisms of polymer-on-polymer surfaces. *Science* **2002**, *297*, 379–382. [[CrossRef](#)] [[PubMed](#)]
58. Greenwood, J.A.; Tripp, J.H. The contact of two nominally flat rough surfaces. *Arch. Proc. Inst. Mech. Eng.* **1970**, *185*, 625–633. [[CrossRef](#)]
59. Cornelissen, B.; de Rooij, M.B.; Rietman, B.; Akkerman, R. Frictional behavior of carbon fiber tows: A contact mechanics model of tow–tow friction. *Text. Res. J.* **2014**, *84*, 1476–1488. [[CrossRef](#)]
60. Cornelissen, B.; de Rooij, M.B.; Rietman, B.; Akkerman, R. Frictional behaviour of high performance fibrous tows: A contact mechanics model of tow-metal friction. *Wear* **2013**, *305*, 78–88. [[CrossRef](#)]
61. Johnson, K.L.; Kendall, K.; Roberts, A.D. Surface Energy and the Contact of Elastic Solids. *Proc. R. Soc. A Math. Phys. Eng. Sci.* **1971**, *324*, 301–313. [[CrossRef](#)]
62. Gupta, B.S.; Bhupender, S. *Friction in Textile Materials*; Woodhead Publishing Limited: Cambridge, UK, 2008; ISBN 9781855739208.
63. Sen, K.R.; Ahmad, N. 23—The clinging power of single cotton fibres in relation to their physical properties. *J. Text. Inst. Trans.* **1938**, *29*, T258–T279. [[CrossRef](#)]
64. Lord, E. Frictional forces between fringes of fibres. *J. Text. Inst. Proc.* **1955**, *46*, P41–P58. [[CrossRef](#)]
65. Du Bois, W.F. Frictional Measurements on Fibrous Materials. *Text. Res. J.* **1959**, *29*, 451–466. [[CrossRef](#)]
66. Belser, R.B.; Taylor, J. *Frictional Properties of Cotton Fibers*; U.S. Department of Agriculture: Washington, DC, USA, 1968.
67. Hertel, K.L.; Lawson, R. Shear friction within multiple card web specimens. *Text. Res. J.* **1970**, *40*, 472–477. [[CrossRef](#)]
68. Viswanathan, A. Some experiments on the friction of cotton fibers. *J. Text. Inst.* **1973**, *64*, 553–557. [[CrossRef](#)]
69. Subramaniam, V.; Sreenivasan, K.; Pillay, K.P.R. Studies in Fibre Friction: Part II-Influence of Fibre Friction on Cohesion, Configuration and Evenness of Fibre Assemblies. *Indian J. Fibre Text. Res.* **1981**, *6*, 16–21.
70. Subramaniam, V.; Sreenivasan, K.; Pillay, K.P.R. Studies in Fibre Friction: Part I-Effect of Friction on Fibre Properties and Processing Performance of Cotton. *Indian J. Fibre Text. Res.* **1981**, *6*, 9–15.
71. El Mogahzy, Y.E.; Broughton, R.M. A new approach for evaluating the frictional behavior of cotton fibers. *Text. Res. J.* **1993**, *63*, 465–475. [[CrossRef](#)]

72. Pesacreta, T.C.; Carlson, L.C.; Triplett, B.A. Atomic force microscopy of cotton fiber cell wall surfaces in air and water: Quantitative and qualitative aspects. *Planta* **1997**, *202*, 435–442. [[CrossRef](#)]
73. El Mogahzy, Y.; Broughton, R.; Hong Guo, H.; Taylor, R.A. Evaluating staple fiber processing propensity. *Text. Res. J.* **1998**, *68*, 835–840. [[CrossRef](#)]
74. Gamble, G.R. Variation in Surface Chemical Constituents of Cotton (*Gossypium hirsutum*) Fiber as a Function of Maturity. *J. Agric. Food Chem.* **2003**, *51*, 7995–7998. [[CrossRef](#)] [[PubMed](#)]
75. Nowrouzieh, S.; Sinoimeri, A.; Drean, J.-Y.; Frydrych, R. A new method of measurement of the interfiber force. *Text. Res. J.* **2007**, *77*, 489–494. [[CrossRef](#)]
76. Zhang, Z.; Fletcher, I.W.; Hurley, C.R.; Boardman, C.; Doyle, P.; Leggett, G.J.; Poutch, F.; Turner, P.S.; Watson, G.S. Morphological and quantitative frictional measurements of cotton fibres using friction force microscopy. *J. Mater. Chem.* **2010**, *20*, 8531–8538. [[CrossRef](#)]
77. Zhang, Y.; Tian, Y.; Meng, Y. Mechanical interlocking of cotton fibers on slightly textured surfaces of metallic cylinders. *Sci. Rep.* **2016**, *6*, 25403. [[CrossRef](#)] [[PubMed](#)]
78. Hosseinali, F.; Thomasson, J.A. Variability of Fiber Friction among Cotton Varieties: Influence of Salient Fiber Physical Metrics. *Tribol. Int.* **2018**, *127*, 433–445. [[CrossRef](#)]
79. Hosseinali, F.; Thomasson, J.A.; Batteas, J.D. Friction Measurements on Cotton Fiber Bundles and Single Fibers. *Membranes* **2018**, *3*, 5.
80. Viswanathan, A. Frictional forces in cotton and regenerated cellulosic fibres. *J. Text. Inst. Trans.* **1966**, *57*, T30–T41. [[CrossRef](#)]
81. Roedel, C.; Ramkumar, S.S. Surface and Mechanical Property Measurements of H Technology Needle-Punched Nonwovens. *Text. Res. J.* **2003**, *73*, 381–385. [[CrossRef](#)]
82. Hertel, K.L. Measurement of Fiber Assembly Shear Energy Transformation. *Text. Res. J.* **1967**, *37*, 433–434. [[CrossRef](#)]
83. El Mogahzy, Y.E. Friction and surface characteristics of cotton fibers. In *Friction in Textile Materials*; Gupta, B., Ed.; Woodhead Publishing Limited: Cambridge, UK, 2008; pp. 225–252.
84. Ghosh, S.; Rodgers, J.E.; Ortega, A.E. RotorRing measurement of fiber cohesion and bulk properties of staple fibers. *Text. Res. J.* **1992**, *62*, 608–613. [[CrossRef](#)]
85. Gamble, G.R. Influence of Surface Electrolyte and Moisture Content on the Frictional Behavior of Cotton Fiber. *J. Cotton Sci.* **2006**, *10*, 61–67.
86. Lewin, M.; Litav, Y.; Shiloh, M. Crimp in cotton: Crimp as a new characteristic of cotton fibres. *Nature* **1962**, *196*, 152–153. [[CrossRef](#)]
87. Hecht, A.; Shiloh, M. Studies on Cotton Crimp: Part I: Comparisons Between the Crimp Parameters of Twelve Varieties of Cotton1. *Text. Res. J.* **1965**, *35*, 539–546. [[CrossRef](#)]
88. Alexander, E.; Litav, Y.; Peres, H. Crimp in Cotton: Some Aspects of the Behaviour of Crimp of Cotton Fibres. *Nature* **1962**, *196*, 153–154. [[CrossRef](#)]
89. Shiloh, M.; Litav, Y. Studies on Cotton Crimp: Part II: The Recovery of Crimp of Cotton Fibers After Successive Loadings. *Text. Res. J.* **1965**, *35*, 546–553. [[CrossRef](#)]
90. Alexander, E.; Lewin, M.; Litav, Y.; Peres, H.; Shiloh, M. The Crimp of Cotton Fibers. *Text. Res. J.* **1962**, *32*, 898–908. [[CrossRef](#)]
91. Israelachvili, J.; Min, Y.; Akbulut, M.; Alig, A.; Carver, G.; Greene, W.; Kristiansen, K.; Meyer, E.; Pesika, N.; Rosenberg, K.; et al. Recent advances in the surface forces apparatus (SFA) technique. *Rep. Prog. Phys.* **2010**, *73*, 36601. [[CrossRef](#)]
92. Binnig, G.; Quate, C.F.; Gerber, C. Atomic Force Microscope. *Phys. Rev. Lett.* **1986**, *56*, 930–933. [[CrossRef](#)] [[PubMed](#)]
93. Bhushan, B.; Israelachvili, J.N.; Landman, U. Nanotribology: Friction, wear and lubrication at the atomic scale. *Nature* **1995**, *374*, 607–616. [[CrossRef](#)]
94. Perry, S.S. Scanning probe microscopy measurements of friction. *MRS Bull.* **2004**, *29*, 478–483. [[CrossRef](#)]
95. Szlufarska, I.; Chandross, M.; Carpick, R.W. Recent advances in single-asperity nanotribology. *J. Phys. D Appl. Phys.* **2008**, *41*, 123001. [[CrossRef](#)]
96. Mathew Mate, C. On the Road to an Atomic- and Molecular-Level Understanding of Friction. *MRS Bull.* **2002**, *27*, 967–971. [[CrossRef](#)]
97. Bhushan, B. Nanotribology and nanomechanics. *Wear* **2005**, *259*, 1507–1531. [[CrossRef](#)]

98. Carpick, R.W.; Salmeron, M. Scratching the Surface: Fundamental Investigations of Tribology with Atomic Force Microscopy. *Chem. Rev.* **1997**, *97*, 1163–1194. [[CrossRef](#)] [[PubMed](#)]
99. Mo, Y.; Turner, K.T.; Szlufarska, I. Friction laws at the nanoscale. *Nature* **2009**, *457*, 1116–1119. [[CrossRef](#)] [[PubMed](#)]
100. Lee, C.; Li, Q.; Kalb, W.; Liu, X.Z.; Berger, H.; Carpick, R.W.; Hone, J. Frictional Characteristics of Atomically Thin Sheets. *Science* **2010**, *328*, 76–80. [[CrossRef](#)] [[PubMed](#)]
101. Brewer, N.J.; Beake, B.D.; Leggett, G.J. Friction Force Microscopy of Self-Assembled Monolayers: Influence of Adsorbate Alkyl Chain Length, Terminal Group Chemistry, and Scan Velocity. *Langmuir* **2001**, *17*, 1970–1974. [[CrossRef](#)]
102. Bliznyuk, V.N.; Everson, M.P.; Tsukruk, V.V. Nanotribological Properties of Organic Boundary Lubricants: Langmuir Films Versus Self-Assembled Monolayers. *J. Tribol.* **1998**, *120*, 489–495. [[CrossRef](#)]
103. Tsukruk, V.V.; Reneker, D.H. Scanning probe microscopy of organic and polymeric films: From self-assembled monolayers to composite multilayers. *Polymer* **1995**, *36*, 1791–1808. [[CrossRef](#)]
104. Tsukruk, V.V. Scanning Probe Microscopy of Polymer Surfaces. *Rubber Chem. Technol.* **1997**, *70*, 430–467. [[CrossRef](#)]
105. Johnson, L.L. Atomic Force Microscopy (AFM) for Rubber. *Rubber Chem. Technol.* **2008**, *81*, 359–383. [[CrossRef](#)]
106. Ruan, J.-A.; Bhushan, B. Atomic-Scale Friction Measurements Using Friction Force Microscopy: Part I—General Principles and New Measurement Techniques. *J. Tribol.* **1994**, *116*, 378–388. [[CrossRef](#)]
107. Bhushan, B.; Ruan, J.-A. Atomic-Scale Friction Measurements Using Friction Force Microscopy: Part II—Application to Magnetic Media. *J. Tribol.* **1994**, *116*, 389–396. [[CrossRef](#)]
108. Haugstad, G.; Gladfelter, W.L.; Jones, R.R. Nanotribology on a polymer network film. *J. Vac. Sci. Technol. A Vac. Surf. Film* **1996**, *14*, 1864–1869. [[CrossRef](#)]
109. Nisman, R.; Smith, P.; Vancso, G.J. Anisotropic Friction at the Surface of Lamellar Crystals of Poly(oxymethylene) by Lateral Force Microscopy. *Langmuir* **1994**, *10*, 1667–1669. [[CrossRef](#)]
110. Bhushan, B.; Koinkar, V.N. Microtribology of PET Polymeric Films. *Tribol. Trans.* **1995**, *38*, 119–127. [[CrossRef](#)]
111. Cho, D.-H.; Bhushan, B. Nanofriction and nanowear of polypropylene, polyethylene terephthalate, and high-density polyethylene during sliding. *Wear* **2016**, *352–353*, 18–23. [[CrossRef](#)]
112. Kumar, A.; Bhushan, B. Effect of Nanoparticles on Nanomechanical and Nanotribological Properties of Polyethylene Blend Films. *Macromol. React. Eng.* **2013**, *7*, 538–548. [[CrossRef](#)]
113. Tambe, N.S.; Bhushan, B. Scale dependence of micro/nano-friction and adhesion of MEMS/NEMS materials, coatings and lubricants. *Nanotechnology* **2004**, *15*, 1561–1570. [[CrossRef](#)]
114. Bogdanovic, G.; Tibergh, F.; Rutland, M.W. Sliding Friction between Cellulose and Silica Surfaces. *Langmuir* **2001**, *17*, 5911–5916. [[CrossRef](#)]
115. Nordgren, N.; Eronen, P.; Österberg, M.; Laine, J.; Rutland, M.W. Mediation of the Nanotribological Properties of Cellulose by Chitosan Adsorption. *Biomacromolecules* **2009**, *10*, 645–650. [[CrossRef](#)] [[PubMed](#)]
116. Haugstad, G.; Gladfelter, W.L.; Weberg, E.B.; Weberg, R.T.; Weatherill, T.D. Probing Biopolymers with Scanning Force Methods: Adsorption, Structure, Properties, and Transformation of Gelatin on Mica. *Langmuir* **1994**, *10*, 4295–4306. [[CrossRef](#)]
117. Haugstad, G.; Gladfelter, W.L.; Weberg, E.B.; Weberg, R.T.; Jones, R.R. Probing molecular relaxation on polymer surfaces with friction force microscopy. *Langmuir* **1995**, *11*, 3473–3482. [[CrossRef](#)]
118. Kajiyama, T.; Tanaka, K.; Takahara, A. Surface Molecular Motion of the Monodisperse Polystyrene Films. *Macromolecules* **1997**, *30*, 280–285. [[CrossRef](#)]
119. Tanaka, K.; Takahara, A.; Kajiyama, T. Effect of Polydispersity on Surface Molecular Motion of Polystyrene Films. *Macromolecules* **1997**, *30*, 6626–6632. [[CrossRef](#)]
120. Hammerschmidt, J.A.; Moasser, B.; Gladfelter, W.L.; Haugstad, G.; Jones, R.R. Polymer Viscoelastic Properties Measured by Friction Force Microscopy. *Macromolecules* **1996**, *29*, 8996–8998. [[CrossRef](#)]
121. Hammerschmidt, J.A.; Gladfelter, W.L.; Haugstad, G. Probing Polymer Viscoelastic Relaxations with Temperature-Controlled Friction Force Microscopy. *Macromolecules* **1999**, *32*, 3360–3367. [[CrossRef](#)]
122. Haugstad, G.; Hammerschmidt, J.A.; Gladfelter, W.L. Viscoelasticity in Nanoscale Friction on Thin Polymer Films. In *Interfacial Properties on the Submicrometer Scale*; Frommer, J., Overney, R.M., Eds.; ACS Symposium Series; American Chemical Society: Washington, DC, USA, 2000; pp. 230–253.

123. Ahimou, F.; Semmens, M.J.; Novak, P.J.; Haugstad, G. Biofilm cohesiveness measurement using a novel atomic force microscopy methodology. *Appl. Environ. Microbiol.* **2007**, *73*, 2897–2904. [[CrossRef](#)] [[PubMed](#)]
124. Aoyama, S.; Park, Y.T.; Macosko, C.W.; Ougizawa, T.; Haugstad, G. AFM Probing of Polymer/Nanofiller Interfacial Adhesion and Its Correlation with Bulk Mechanical Properties in a Poly(ethylene terephthalate) Nanocomposite. *Langmuir* **2014**, *30*, 12950–12959. [[CrossRef](#)] [[PubMed](#)]
125. Brown, H.R. Chain Pullout and Mobility Effects in Friction and Lubrication. *Science* **1994**, *263*, 1411–1413. [[CrossRef](#)] [[PubMed](#)]
126. Chen, N.; Maeda, N.; Tirrell, M.; Israelachvili, J. Adhesion and Friction of Polymer Surfaces: The Effect of Chain Ends. *Macromolecules* **2005**, *38*, 3491–3503. [[CrossRef](#)]
127. Zeng, H.; Maeda, N.; Chen, N.; Tirrell, M.; Israelachvili, J. Adhesion and Friction of Polystyrene Surfaces around  $T_g$ . *Macromolecules* **2006**, *39*, 2350–2363. [[CrossRef](#)]
128. Butt, H.-J.; Cappella, B.; Kappl, M. Force measurements with the atomic force microscope: Technique, interpretation and applications. *Surf. Sci. Rep.* **2005**, *59*, 1–152. [[CrossRef](#)]
129. Burnham, N.A.; Colton, R.J.; Pollock, H.M. Interpretation of force curves in force microscopy. *Nanotechnology* **1993**, *4*, 64–80. [[CrossRef](#)]
130. Leckband, D.; Israelachvili, J. Intermolecular forces in biology. *Q. Rev. Biophys.* **2001**, *34*, 105–267. [[CrossRef](#)] [[PubMed](#)]
131. McConney, M.E.; Singamaneni, S.; Tsukruk, V.V. Probing Soft Matter with the Atomic Force Microscopies: Imaging and Force Spectroscopy. *Polym. Rev.* **2010**, *50*, 235–286. [[CrossRef](#)]
132. Cappella, B. Mechanical Properties and Adhesion of a Micro Structured Polymer Blend. *Polymers* **2011**, *3*, 1091–1106. [[CrossRef](#)]
133. Alessandrini, A.; Facci, P. AFM: A versatile tool in biophysics. *Meas. Sci. Technol.* **2005**, *16*, R65–R92. [[CrossRef](#)]
134. Heinz, W.F.; Hoh, J.H. Spatially resolved force spectroscopy of biological surfaces using the atomic force microscope. *Trends Biotechnol.* **1999**, *17*, 143–150. [[CrossRef](#)]
135. Milani, P.; Braybrook, S.A.; Boudaoud, A. Shrinking the hammer: Micromechanical approaches to morphogenesis. *J. Exp. Bot.* **2013**, *64*, 4651–4662. [[CrossRef](#)] [[PubMed](#)]
136. Ehrhardt, D.W.; Frommer, W.B. New technologies for 21st century plant science. *Plant Cell* **2012**, *24*, 374–394. [[CrossRef](#)] [[PubMed](#)]
137. Batteas, J.D.; Stark, R.E. Surface and interfacial studies of plant biopolymers. In *Molecular Interfacial Phenomena of Polymers and Biopolymers*; Elsevier: New York, NY, USA, 2005; pp. 580–608.
138. Batteas, J.D.; Quan, X.; Weldon, M.K. Adhesion and wear of colloidal silica probed by force microscopy. *Tribol. Lett.* **1999**, *7*, 121–128. [[CrossRef](#)]
139. Kawai, A.; Nagata, H.; Takata, M. Characterization of Surface Energetic Behavior by Atomic Force Microscopy. *Jpn. J. Appl. Phys.* **1992**, *31*, L977–L979. [[CrossRef](#)]
140. Blackman, G.S.; Mate, C.M.; Philpott, M.R. Interaction forces of a sharp tungsten tip with molecular films on silicon surfaces. *Phys. Rev. Lett.* **1990**, *65*, 2270–2273. [[CrossRef](#)] [[PubMed](#)]
141. Mate, C.M.; Lorenz, M.R.; Novotny, V.J. Atomic force microscopy of polymeric liquid films. *J. Chem. Phys.* **1989**, *90*, 7550–7555. [[CrossRef](#)]
142. Bhushan, B.; Dandavate, C. Thin-film friction and adhesion studies using atomic force microscopy. *J. Appl. Phys.* **2000**, *87*, 1201–1210. [[CrossRef](#)]
143. Mizes, H.A.; Loh, K.-G.; Miller, R.J.D.; Ahuja, S.K.; Grabowski, E.F. Submicron probe of polymer adhesion with atomic force microscopy: Dependence on topography and material inhomogeneities. *Appl. Phys. Lett.* **1991**, *59*, 2901–2903. [[CrossRef](#)]
144. Sirghi, L.; Nakagiri, N.; Sugisaki, K.; Sugimura, H.; Takai, O. Effect of Sample Topography on Adhesive Force in Atomic Force Spectroscopy Measurements in Air. *Langmuir* **2000**, *16*, 7796–7800. [[CrossRef](#)]
145. Eaton, P.; Estarlich, F.F.; Ewen, R.J.; Nevell, T.G.; Smith, J.R.; Tsibouklis, J. Combined Nanoindentation and Adhesion Force Mapping Using the Atomic Force Microscope: Investigations of a Filled Polysiloxane Coating. *Langmuir* **2002**, *18*, 10011–10015. [[CrossRef](#)]
146. Eaton, P.; Smith, J.R.; Graham, P.; Smart, J.D.; Nevell, T.G.; Tsibouklis, J. Adhesion Force Mapping of Polymer Surfaces: Factors Influencing Force of Adhesion. *Langmuir* **2002**, *18*, 3387–3389. [[CrossRef](#)]

147. Eaton, P.J.; Graham, P.; Smith, J.R.; Smart, J.D.; Nevell, T.G.; Tsibouklis, J. Mapping the Surface Heterogeneity of a Polymer Blend: An Adhesion-Force-Distribution Study Using the Atomic Force Microscope. *Langmuir* **2000**, *16*, 7887–7890. [[CrossRef](#)]
148. Begat, P.; Morton, D.A.V.; Staniforth, J.N.; Price, R. The Cohesive-Adhesive Balances in Dry Powder Inhaler Formulations I: Direct Quantification by Atomic Force Microscopy. *Pharm. Res.* **2004**, *21*, 1591–1597. [[CrossRef](#)] [[PubMed](#)]
149. Mangipudi, V.; Tirrell, M.; Pcius, A.V. Direct measurement of molecular level adhesion between poly(ethylene terephthalate) and polyethylene films: Determination of surface and interfacial energies. *J. Adhes. Sci. Technol.* **1994**, *8*, 1251–1270. [[CrossRef](#)]
150. Merrill, W.W.; Pocius, A.V.; Thakker, B.V.; Tirrell, M. Direct measurement of molecular level adhesion forces between biaxially oriented solid polymer films. *Langmuir* **1991**, *7*, 1975–1980. [[CrossRef](#)]
151. Tirrell, M. Measurement of Interfacial Energy at Solid Polymer Surfaces. *Langmuir* **1996**, *12*, 4548–4551. [[CrossRef](#)]
152. Baselt, D.R.; Baldeschwieler, J.D. Imaging spectroscopy with the atomic force microscope. *J. Appl. Phys.* **1994**, *76*, 33–38. [[CrossRef](#)]
153. Rosa-Zeiser, A.; Weilandt, E.; Hild, S.; Marti, O. The simultaneous measurement of elastic, electrostatic and adhesive properties by scanning force microscopy: Pulsed-force mode operation. *Meas. Sci. Technol.* **1997**, *8*, 1333–1338. [[CrossRef](#)]
154. Rezende, C.A.; Lee, L.-T.; Galembeck, F. Surface Mechanical Properties of Thin Polymer Films Investigated by AFM in Pulsed Force Mode. *Langmuir* **2009**, *25*, 9938–9946. [[CrossRef](#)] [[PubMed](#)]
155. Chyasnavichyus, M.; Young, S.L.; Tsukruk, V.V. Mapping micromechanical properties of soft polymer contact lenses. *Polymer* **2014**, *55*, 6091–6101. [[CrossRef](#)]
156. Foster, B. New Atomic Force Microscopy (AFM) Approaches Life Sciences Gently, Quantitatively, and Correlatively. *Am. Lab.* **2012**, *44*, 24–28.
157. Zhang, S.; Aslan, H.; Besenbacher, F.; Dong, M. Quantitative biomolecular imaging by dynamic nanomechanical mapping. *Chem. Soc. Rev.* **2014**, *43*, 7412–7429. [[CrossRef](#)] [[PubMed](#)]
158. Dufrène, Y.F.; Martínez-Martín, D.; Medalsy, I.; Alsteens, D.; Müller, D.J. Multiparametric imaging of biological systems by force-distance curve-based AFM. *Nat. Methods* **2013**, *10*, 847–854. [[CrossRef](#)] [[PubMed](#)]
159. Bargel, H.; Koch, K.; Cerman, Z.; Neinhuis, C. Structure-function relationships of the plant cuticle and cuticular waxes—A smart material? *Funct. Plant Biol.* **2006**, *33*, 893–910. [[CrossRef](#)]
160. Domínguez, E.; Cuartero, J.; Heredia, A. An overview on plant cuticle biomechanics. *Plant Sci.* **2011**, *181*, 77–84. [[CrossRef](#)] [[PubMed](#)]
161. Domínguez, E.; Heredia-Guerrero, J.A.; Heredia, A. The biophysical design of plant cuticles: An overview. *New Phytol.* **2011**, *189*, 938–949. [[CrossRef](#)] [[PubMed](#)]
162. Mirabet, V.; Das, P.; Boudaoud, A.; Hamant, O. The Role of Mechanical Forces in Plant Morphogenesis. *Annu. Rev. Plant Biol.* **2011**, *62*, 365–385. [[CrossRef](#)] [[PubMed](#)]
163. Koch, K.; Neinhuis, C.; Ensikat, H.; Barthlott, W. Self assembly of epicuticular waxes on living plant surfaces imaged by atomic force microscopy (AFM). *J. Exp. Bot.* **2004**, *55*, 711–718. [[CrossRef](#)] [[PubMed](#)]
164. Round, A.N.; MacDougall, A.J.; Ring, S.G.; Morris, V.J. Unexpected branching in pectin observed by atomic force microscopy. *Carbohydr. Res.* **1997**, *303*, 251–253. [[CrossRef](#)]
165. Round, A.N.; Rigby, N.M.; MacDougall, A.J.; Ring, S.G.; Morris, V.J. Investigating the nature of branching in pectin by atomic force microscopy and carbohydrate analysis. *Carbohydr. Res.* **2001**, *331*, 337–342. [[CrossRef](#)]
166. Chatterjee, S.; Sarkar, S.; Oktawiec, J.; Mao, Z.; Niitsoo, O.; Stark, R.E. Isolation and biophysical study of fruit cuticles. *J. Vis. Exp.* **2012**. [[CrossRef](#)] [[PubMed](#)]
167. Round, A.N.; Yan, B.; Dang, S.; Estephan, R.; Stark, R.E.; Batteas, J.D. The Influence of Water on the Nanomechanical Behavior of the Plant Biopolyester Cutin as Studied by AFM and Solid-State NMR. *Biophys. J.* **2000**, *79*, 2761–2767. [[CrossRef](#)]
168. Bhushan, B.; Jung, Y.C. Micro- and nanoscale characterization of hydrophobic and hydrophilic leaf surfaces. *Nanotechnology* **2006**, *17*, 2758–2772. [[CrossRef](#)]
169. Flint, A.E. The structure and development of the cotton fibre. *Biol. Rev.* **1950**, *25*, 414–434. [[CrossRef](#)]
170. Hartzell-Lawson, M.M.; Hsieh, Y.-L. Characterizing the noncellulosics in developing cotton fibers. *Text. Res. J.* **2000**, *70*, 810–819. [[CrossRef](#)]

171. Vaughn, K.C.; Turley, R.B. The primary walls of cotton fibers contain an ensheathing pectin layer. *Protoplasma* **1999**, *209*, 226–237. [[CrossRef](#)]
172. Brushwood, D.E. Noncellulosic constituents on raw cotton and their relationship to fiber physical properties. *Text. Res. J.* **2003**, *73*, 912–916. [[CrossRef](#)]
173. Cui, X.L.; Price, J.B.; Calamari, T.A.; Hemstreet, J.M.; Meredith, W. Cotton Wax and Its Relationship with Fiber and Yarn Properties. *Text. Res. J.* **2002**, *72*, 399–404. [[CrossRef](#)]
174. Marsh, P.B.; Barker, H.D.; Kerr, T.; Butler, M.L. Wax Content as Related to Surface Area of Cotton Fibers. *Text. Res. J.* **1950**, *20*, 288–297. [[CrossRef](#)]
175. Maxwell, J.M.; Gordon, S.G.; Huson, M.G. Internal Structure of Mature and Immature Cotton Fibers Revealed by Scanning Probe Microscopy. *Text. Res. J.* **2003**, *73*, 1005–1012. [[CrossRef](#)]
176. Koc, S.K. Applications of Atomic Force Microscopy in Textiles. *J. Eng. Fibers Fabr.* **2015**, *10*, 169–173.
177. Lee, I.; Evans, B.R.; Woodward, J. The mechanism of cellulase action on cotton fibers: Evidence from atomic force microscopy. *Ultramicroscopy* **2000**, *82*, 213–221. [[CrossRef](#)]



© 2018 by the authors. Licensee MDPI, Basel, Switzerland. This article is an open access article distributed under the terms and conditions of the Creative Commons Attribution (CC BY) license (<http://creativecommons.org/licenses/by/4.0/>).